

PanMatch: Unleashing the Potential of Large Vision Models for Unified Matching Models

Yongjian Zhang, Longguang Wang, Kunhong Li, Ye Zhang, Yun Wang, Liang Lin, *Fellow, IEEE*, Yulan Guo*

Abstract—This work presents *PanMatch*, a versatile foundation model for robust correspondence matching. Unlike previous methods that rely on task-specific architectures and domain-specific fine-tuning to support tasks like stereo matching, optical flow or feature matching, our key insight is that any two-frame correspondence matching task can be addressed within a 2D displacement estimation framework using the same model weights. Such a formulation eliminates the need for designing specialized unified architectures or task-specific ensemble models. Instead, it achieves multi-task integration by endowing displacement estimation algorithms with unprecedented generalization capabilities. To this end, we highlight the importance of a robust feature extractor applicable across multiple domains and tasks, and propose the *feature transformation pipeline* that leverage all-purpose features from Large Vision Models to endow matching baselines with zero-shot cross-view matching capabilities. Furthermore, we assemble a cross-domain dataset with near *1.8 million samples* from stereo matching, optical flow, and feature matching domains to pretrain PanMatch. We demonstrate the versatility of PanMatch across a wide range of domains and downstream tasks using *the same model weights*. Our model outperforms UniMatch and Flow-Anything on cross-task evaluations, and achieves comparable performance to most state-of-the-art task-specific algorithms on task-oriented benchmarks. Additionally, PanMatch presents unprecedented zero-shot performance in abnormal scenarios, such as rainy day and satellite imagery, where most existing robust algorithms fail to yield meaningful results.

Index Terms—Stereo Matching, Optical Flow Estimation, Feature Matching, Depth Estimation, Domain Generalization.



1 INTRODUCTION

FINDING correspondences in viewpoint-overlapping images is one of the key ways to achieve 3D scene perception and reconstruction. This technique serves as the foundation for various real-world applications, including stereo matching for driving and navigation, optical flow for video editing and action recognition, and feature matching for 3D reconstruction.

Previous research developed specialized architectures and model weights for specific correspondence tasks due to significant difference in task settings, as outlined in Table 1. For instance, stereo matching operates on a pair of synchronized, rectified images and identifies correspondences along horizontal epipolar lines. Feature matching focus on finding reliable correspondence of rigid scenes from varying camera poses and times. Optical flow estimates pixel-wise displacements in dynamic scenes over consecutive frames. Using task-specific priors to construct models simplifies network design and enhances inference efficiency. However, these individual pipelines inherently limits the adaptability of the algorithms across tasks, resulting in numerous specialized architectures and weights for different scenarios, which complicates real-world deployment. Additionally, robust

geometric priors learned from diverse data sources cannot be seamlessly integrated into a single model during training.

Given the inherent similarities across stereo matching, optical flow, and feature matching, several efforts have been made to address correspondence matching within a unified architecture [1], [2]. However, due to task- and domain-specific biases, directly applying these methods across different tasks results in relatively low performance. This raises a question: Can we develop a truly unified model for all correspondence tasks using the same weights?

Drawing from the success of large vision models in other fields [3], we summarize the major challenges of developing such a unified model as twofold. (i) Although most correspondence matching models follow a similar four-step pipeline—feature extraction, cross-view correlation, global cost optimization, and target regression—most methods encode task-specific geometric inductive biases to formulate task-dependent cost volumes [1], followed by target-dependent aggregation networks for regression. This task-relevant design and inconsistent output targets hinder the unification of different correspondence-matching tasks into a single architecture. (ii) Previous methods are pretrained on task-specific and scale-limited datasets, which inevitably leads to domain-sensitive representations and limited generalization capability [4]. Although several works augment their generalization through mixed training datasets [2], they still rely on task-oriented samples, failing to meet the in-the-wild demands of cross-domain and cross-task applications.

To address the first challenge, we construct a unified model by removing task-specific geometric priors and relaxing the problem to a pure all-pairs correspondence matching task, which can be implemented using standard optical flow

- *Corresponding author: Yulan Guo.
- Yongjian Zhang, Longguang Wang, Kunhong Li, Ye Zhang and Yulan Guo are with the School of Electronics and Communication Engineering, the Shenzhen Campus of Sun Yat-sen University, Sun Yat-sen University, Shenzhen, China (e-mail: zhangyj85@mail2.sysu.edu.cn, wanglongguang15@nuict.edu.cn, likh25@mail2.sysu.edu.cn, zhangy2658@sysu.edu.cn, guoyulan@sysu.edu.cn).
- Liang Lin is with the School of Computer Science and Engineering, Sun Yat-sen University, Guangzhou, China (e-mail: linliang@ieee.org). Yun Wang is with the Department of Computer Science, City University of Hong Kong, Kowloon 999077, Hong Kong SAR, China (e-mail: ywang3875-c@my.cityu.edu.hk).

TABLE 1: Comparisons on different correspondence matching tasks.

Task	Focus	Image Pair	Target
Stereo Matching	Static Scenes	Similar	Dense
Feature Matching	Rigid Scenes	Varying	Semi-Dense
Optical Flow	Dynamic Scenes	Similar	Dense

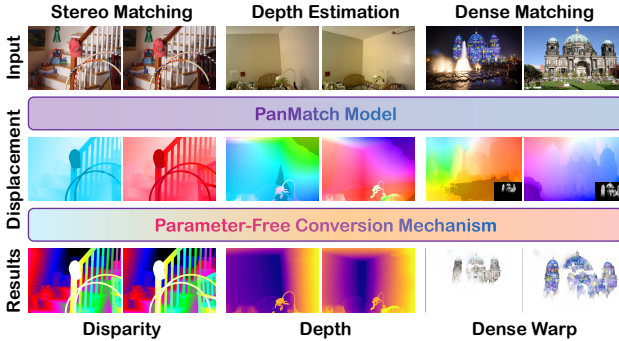


Fig. 1: An overview of the proposed unified architecture. We first estimate the reliable 2D displacement field with PanMatch, and then derive the target correspondence format by parameter-free calculations.

estimation approaches. By this way, the core challenge of developing a unified architecture shifts toward endowing an optical flow baseline with generalization capabilities across tasks and domains. To this end, we emphasize the importance of *robust feature representations*, and leverage large vision models (LVMs) as a feasible solution. We design a feature transformation pipeline, which transfer the multi-layer all-purpose features extracted by LVM into matching-specific representations. This is achieved through a guided feature upsampling block for detail restoration and a lightweight fusion adapter for feature transfer. By integrating these designs, the optical flow baseline can be extended to a unified model capable of both cross-domain generalization and cross-task adaptability.

To address the second challenge, we reorganize various correspondence matching datasets to support our unified matching formulation, thereby expanding the scale and diversity of available training data. In practice, we collect nearly 1.8 million samples from existing datasets developed for stereo matching [5], [6], optical flow [7], [8], [9], [10], [11] and depth estimation [12], [13]. Note that, our dataset is of higher quality and diversity compared with croco v2 [14], StereoAnything [15] and FoundationStereo [16]. Moreover, as our data reorganization strategy is applicable to crowd-sourced matching datasets, it can incorporate newer datasets mentioned above to achieve even larger scales for learning correspondence matching.

We have experimentally demonstrated that leveraging representations from LVMs enhances the cross-domain generalization ability of unified models. Furthermore, the integration of large-scale multi-task training data substantially improves model adaptability across diverse tasks. Based on our unified task formulation and dual advances in model design and data strategy, we develop PanMatch, a versatile foundation model that achieves state-of-the-art performance across multiple benchmarks using identical model weights,

as illustrated in Fig. 1. Our PanMatch achieves the best performance on ETH3D and Spring benchmarks, and ranks second on Middlebury, Sintel and WxBS benchmark when compared to task-specific robust algorithms, demonstrating strong cross-task generalization.

This work significantly extends our previous ECCV 2024 conference paper, *FormerStereo* [17], with the following new contributions:

- We analyze the challenges of unifying diverse correspondence matching tasks and summarize the limitations of existing unified methods.
- We propose to unify any two-view matching task as all-pairs pixel matching paradigm, and extend FormerStereo to optical flow baselines to develop a unified matching model.
- We emphasize the importance of large-scale, high-quality training data, and collect 1.8 million cross-task samples for pretraining.
- We introduce *PanMatch*, the first versatile foundation model capable of addressing diverse correspondence matching tasks, including stereo matching, optical flow estimation, feature matching and depth estimation. Experimental results demonstrate its cross-domain and cross-task zero-shot capabilities, achieving performance comparable to task-specific state-of-the-art (SOTA) methods.

2 RELATED WORK

In this section, we focus on three matching tasks, including stereo matching (Sec. 2.1), optical flow estimation (Sec. 2.2) and feature matching (Sec. 2.3). We also review the applications of LVM in two-view tasks (Sec. 2.4).

2.1 Stereo Matching

In the past decade, learning-based methods have gradually become the dominant approach in stereo matching [18], [19]. Early techniques [20], [21] replace partial steps in the traditional stereo matching pipeline [22] with networks to alleviate the reliance on handcrafted optimization [23]. Since the success of DispNet [7], end-to-end networks with data-driven optimization have gained popularity, with subsequent research focusing on enhancing performance and efficiency through advanced model designs. These approaches primarily improve cost aggregation algorithms [24], [25], [26], [27] or disparity refinement networks [28], [29], [30], [31], [32] for in-domain performance, while overlooking cross-domain applicability. Motivated by the impressive generalization capabilities of RAFT [33] in optical flow estimation, Lipson *et al.* [34] adapted this technique for stereo matching. Building on the RAFT architecture, subsequent approaches [5], [35], [36] mainly focus on enhancing context understanding and accelerating iterative convergence. Nevertheless, the generalization performance of these methods heavily depends on the seen context, which may fail in unseen domains.

Alongside efforts to fine-tune models for target domains, some research has aimed to improve the generalization performance to unseen domains without fine-tuning. Zhang

et al. [37] suggested that learning domain-invariant representations is crucial for generalization. To this end, they proposed domain normalization and SGF layers to reduce domain-sensitive local details. Cai *et al.* [38] employed handcrafted descriptors instead of trainable feature extractors to avoid domain-sensitive information. Liu *et al.* [39] employed frozen, broad-spectrum, task-oriented features to construct a general cosine similarity cost space, thereby mitigating the influence of feature variability on the matching distribution. Zhang *et al.* [40] utilized contrastive learning to enhance feature similarity between matching pixels while penalizing mismatched regions to avoid ambiguous feature representations. Chuah *et al.* [4], [41] argued that shortcut information hinders generalization. Therefore, they obtain shortcut-invariant features by enhancing representation consistency learning for shortcut perturbation. Chang *et al.* [42] further proposed a hierarchical visual transformation training framework with adversarial learning to mitigate shortcuts. Rao *et al.* [43] adopted mask representation learning as an auxiliary task for the feature extractor in stereo matching, improving generalization performance and stability. These methods have advanced the development of generalized stereo matching algorithms by emphasizing robust feature representations. However, learning domain-invariant features from limited data remains a significant challenge, and the additional modules and multitask settings inevitably impacts the in-domain accuracy of baseline methods.

2.2 Optical Flow

Optical flow refers to the 2D motion of pixels from one frame to the next in a video. Traditional methods [44] regard this task as an energy minimization problem, utilizing preset human-defined priors to obtain general solutions. With the emergence of deep learning, model design and data collection have replaced handcrafted priors and features, becoming central to performance improvements. Over the past decade, Dosovitskiy *et al.* [8] pioneered an end-to-end CNN network to directly regress optical flow within a data-driven pipeline, which is followed by subsequent works [7], [45], [46]. Recently, Teed *et al.* [33] introduced RAFT, a novel architecture that iteratively updates flow estimations to achieve generalizable estimation, setting a new baseline to the community [47], [48]. Nonetheless, these methods still struggle with small and fast-moving objects, which require global correlation rather than local cost volumes. To overcome this limitation, Xu *et al.* [1], [49] leveraged Transformers to develop a robust feature extractor, enabling the direct estimation of optical flow from an all-pairs correlation volume. Huang *et al.* [50] processed the all-pairs correlation volume with Transformers to obtain a global cost memory, providing global cues for flow estimations. Since RAFT, generalization performance has been increasingly valued, yet most methods still heavily rely on fine-tuning to achieve optimal performance on the Sintel [51] and KITTI [52] benchmarks.

The data-driven learning paradigm has also spawned numerous open-source optical flow datasets. Dosovitskiy *et al.* [8] proposed the first large-scale FlyingChair dataset. Then, Mayer *et al.* [7] introduced a more realistic FlyingThings dataset. Sun *et al.* [9] proposed a self-optimizing data

generation pipeline that synthesizes pretraining data to boost baseline performance on the Sintel [51] benchmark. Additionally, researchers in the fields like SLAM [11], autonomous driving [10], [52], [53], [54], and data generation [55] create datasets with additional optical flow annotation, significantly increasing the quantity of training data for optical flow estimation. However, existing optical flow annotations focus on continuous motion of dynamic objects, ignoring the complex real-world scenarios, such as non-Lambertian reflections and significant differences in viewing angles caused by high-speed camera motion.

2.3 Feature Matching

Feature matching can be categorized into detector-based and detector-free methods. Previous research [56], [57], [58], [59] predominantly focuses on detector-based strategies, which first detect keypoints that are robust to significant appearance and viewpoint variations, thereby reducing potential matching noise caused by ambiguous features. After detection, feature description and all-pairs matching strategies are used to identify reliable correspondences. However, these multi-stage strategies heavily rely on the quality of detected keypoints and may fail when their quantity is insufficient, distinctiveness is ambiguous, or localization precision is compromised. Recent advancements bypass point detection and perform dense, pixel-wise matching on low-resolution feature maps [60], [61]. To further enhance accuracy and robustness, these methods focus on developing more robust feature descriptors [62], [63], improving global matching strategies [64], or incorporating fine-grained refinement techniques [63]. For instance, Sun *et al.* [62], [65] employed linear Transformers across views to augment low-resolution feature descriptions with global context, enhancing the robustness of the descriptors in textureless regions. Edstedt *et al.* [63] replaced traditional CNNs with the frozen DINOv2 [66], yielding more robust coarse feature descriptions. In line with these approaches, our method leverages large vision models to obtain robust feature representations across all scales.

Unlike aforementioned methods that filter unreliable points before matching, recent research jointly estimates all-pairs correspondences with confidence, following post-matching filtering to discard unreliable pairs. Zhang *et al.* [2] designed an uncertainty network to mask unreliable optical flow predictions in occluded or homogeneous regions. Wannenwetsch *et al.* [44] converted energy functions into Gibbs distributions to jointly model optical flow and uncertainty. Yin *et al.* [67] treated the motion of each pixel as a discrete random variable, using a discrete probability distribution to calculate both optical flow and uncertainty. Wang *et al.* [48] adopted mixture Laplacian parameterized distributions for probabilistic modeling. Truong *et al.* [68], [69] parameterized predictive distributions as constrained mixture models to jointly represent accurate predictions and outliers. Additionally, they introduced an uncertainty decoder to address overconfidence in estimation results. These methods demonstrate that confidence estimation can be integrated into optical flow frameworks for dense feature matching. Inspired by these advances, we also employ a two-stage approach for feature matching, involving pixel-wise matching followed by filtering of unreliable estimates.

2.4 LVMS' Application on Correspondence Matching

Inspired by the rapid development of large vision models like CLIP [70], SAM [71] and DAM [72], recent researchers try to expend their applications to downstream tasks through partial parameter fine-tuning [73], [74]. However, such works mainly focus on the single-view tasks like detection and segmentation. Recently, Zhang *et al.* [17] adopted frozen LVMS for domain generalized stereo matching. Liu *et al.* [75] also leveraged the frozen LVM representations as the input, and designed an elaborate cross-view enhance module to achieve task adaptation for stereo matching. Bartolomei *et al.* [76] proposed StereoAnywhere, leveraging the normal priors in DAMv2 [77] to enhance the generalized capacity of RAFT-Stereo. Zhou *et al.* [78] utilized the frozen SAM [71] backbone to enhance the context representations, which facilitates the generalization ability to the fragmentation attack scenes. Edstedt *et al.* [63] treated the frozen DINOv2 as the robust but coarse feature matcher for dense feature matching. Different from these methods that treat LVM features as auxiliary priors to enhance task-specific in-domain performance, we focus on unleashing the potential of LVM for cross-domain multi-task matching capabilities.

3 UNIFIED MATCHING FORMULATION

In this section, we present our unified matching formulation. Specifically, we first discuss why different correspondence tasks can be unified as a single problem in Sec. 3.1. Then, we introduce how to derive task-specific geometric correspondences from the unified representation in Sec. 3.2.

3.1 Unified Representation

Intuitively, unifying two-frame correspondence tasks requires a unified representation to accommodate various types of geometric correspondences, such as disparity, flow, depth, and keypoint correspondences. Our key insight is that all these tasks can be formulated as all-pairs pixel matching problems, since they share a common objective of establishing geometric correspondences between pixels. Specifically, stereo matching and unrectified stereo depth estimation can be viewed as 1D displacement estimation problems along epipolar lines. Optical flow estimation corresponds to a 2D displacement estimation problem, while feature matching involves an additional confidence filtering step to yield sparse but reliable 2D displacement estimation. These tasks differ only in the bias of displacement distribution and task-specific priors (*e.g.*, epipolar constraints, photometric consistency assumption, and keypoint distinctiveness). From this point of view, these tasks can be formulated as the prior-free prediction of pixel-wise 2D displacement field $(\Delta u, \Delta v)$. Such a unified 2D displacement formulation eliminates the need for designing specialized unified architectures or task-specific ensemble models, allowing for constructing a versatile foundation model for robust correspondence matching.

3.2 Conversion Mechanism

Given a pair of images $\mathcal{I} = \{\mathbf{I}_{ref}, \mathbf{I}_{tar}\}$, our unified formulation aims at finding the pixel-wise correspondences from

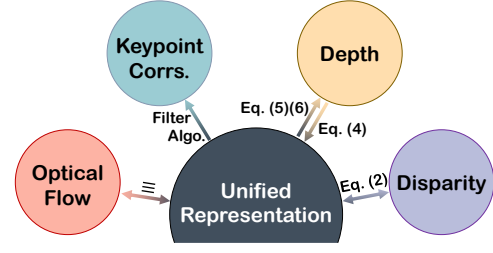


Fig. 2: Conversion mechanism.

the reference image to the target one. These correspondences are represented using pixel coordinate displacements as:

$$\mathbf{I}_{ref}(u_1, v_1) = \mathbf{I}_{tar}(u_2 - \Delta u, v_2 - \Delta v), \quad (1)$$

where $(\Delta u, \Delta v)$ denotes the ground-truth displacement vector from the reference image $\mathbf{I}_{ref}(u_1, v_1)$ to the target one $\mathbf{I}_{tar}(u_2, v_2)$. This representation is consistent with the standard definition of optical flow, therefore, the displacement field can directly serve as the output of optical flow task. Similarly, keypoint correspondences required for feature matching can be derived from the dense displacement field through post-processing, such as applying forward-backward cyclic consistency to extract correspondences within the overlapping view region.

Moreover, if the image pair is a rectified stereo pair, with the reference image corresponding to the left view, the disparity can be derived from the displacement as:

$$\Delta D = -\Delta u, \Delta v = 0, \quad (2)$$

since disparity is defined as

$$\mathbf{I}_{ref}(u_1, v_1) = \mathbf{I}_{tar}(u_2 + \Delta D, v_2), \quad (3)$$

where ΔD denotes the ground-truth disparity. Additionally, if the pair is captured in a regular static scene without moving objects, the scene depth can be inferred using the known camera pose $[\mathbf{R} \ \mathbf{T}]$ and intrinsics \mathbf{K} according to the pinhole camera projection model:

$$\begin{bmatrix} u_2 \\ v_2 \\ 1 \end{bmatrix} = \mathbf{K}_2(\mathbf{R}_2\mathbf{R}_1^{-1}(\mathbf{K}_1^{-1} \begin{bmatrix} u_1 \\ v_1 \\ 1 \end{bmatrix} Z - \mathbf{T}_1) + \mathbf{T}_2), \quad (4)$$

where $u_2 = u_1 + \Delta u$, $v_2 = v_1 + \Delta v$. By defining $\mathbf{H} = \mathbf{K}_2\mathbf{R}_2\mathbf{R}_1^{-1}\mathbf{K}_1^{-1}$, $\mathbf{B} = -\mathbf{K}_2\mathbf{R}_2\mathbf{R}_1^{-1}\mathbf{T}_1 + \mathbf{K}_2\mathbf{T}_2$, we simplify the matrix and can infer the pixel-wise depth as

$$Z_u(u_1, v_1) = \frac{B_{31}u_2 - B_{11}}{(H_{11}u_1 + H_{12}v_1 + H_{13}) - (H_{31}u_1 + H_{32}v_1 + H_{33})u_2}, \quad (5)$$

or

$$Z_v(u_1, v_1) = \frac{B_{31}v_2 - B_{21}}{(H_{21}u_1 + H_{22}v_1 + H_{23}) - (H_{31}u_1 + H_{32}v_1 + H_{33})v_2}. \quad (6)$$

Theoretically, the depths calculated using Eq. 5 or Eq. 6 should be consistent. However, they may not align in practice due to the matching noise and calibration errors. To address this inconsistency, we optimize $Z(u_1, v_1)$ using least squares as $Z_{lsm}(u_1, v_1) = (\mathbf{A}^T \mathbf{A})^{-1} \mathbf{A}^T \mathbf{b}$, where

$$\mathbf{A} = \begin{bmatrix} (H_{11}u_1 + H_{12}v_1 + H_{13}) - (H_{31}u_1 + H_{32}v_1 + H_{33})u_2 \\ (H_{21}u_1 + H_{22}v_1 + H_{23}) - (H_{31}u_1 + H_{32}v_1 + H_{33})v_2 \end{bmatrix}, \quad (7)$$

$$\mathbf{b} = \begin{bmatrix} B_{31}u_2 - B_{11} \\ B_{31}v_2 - B_{21} \end{bmatrix}. \quad (8)$$

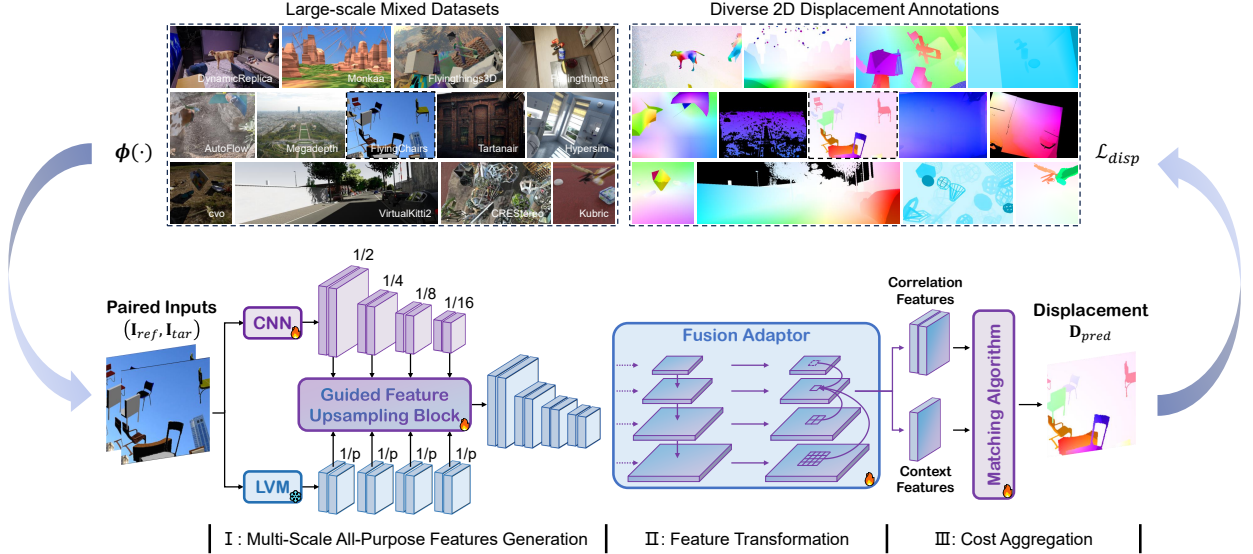


Fig. 3: An overview of the proposed framework. $\phi(\cdot)$ means data augmentation strategies described in Sec. 5.1.

4 UNIFIED MATCHING MODEL

With the aforementioned unified formulation, as well as its representational equivalence to optical flow, we develop a unified model based on existing optical flow baselines. However, the limited feature representation capacity of these baselines compromises cross-task and cross-domain generalization. Motivated by the impressive zero-shot performance of LVMs on diverse downstream applications [17], [63], [78], we leverage LVMs to build a general and robust feature extractor to achieve generalization gains. In particular, we regard all-purpose features produced by ViT-based foundation models [66], [71], [72] as domain-invariant representations, and adapt such features for the dense correspondence task.

We provide an overview of our proposed framework in Fig. 3, which can be separated into three parts: multi-scale all-purpose feature generation, feature transformation, and cost aggregation. Specifically, given a pair of images $\mathcal{I} = \{I_{ref}, I_{tar}\}$, we first obtain the multi-scale features $\{G_{1/2}, G_{1/4}, G_{1/8}, G_{1/16}\}$ from CNN and multi-layer all-purposed features $\{F_{l_1}, F_{l_2}, F_{l_3}, F_{l_4}\}$ from ViT-based foundation model, respectively. The CNN features guide the interpolation of the plain ViT features into pyramid ones via the guided upsampling module. These pyramid features are subsequently processed by a feature pyramid network (FPN) for multi-scale integration and task transfer. Finally, the resultant multi-scale feature pyramid is adapted to a specific matching baseline for displacement estimation.

In the following, we will first demonstrate our motivation that LVMs are superior to encoders trained on small-scale, task-specific datasets for multi-domain generalization in Sec. 4.1. Then, we introduce our feature transformation strategy for adapting LVMs to matching models, including the module design and loss constraints in Sec. 4.2. We finally present the loss function in Sec. 4.3.

4.1 Motivation

We first investigate whether all-purpose features offer advantages over task-specific features in cross-domain match-

TABLE 2: Toy Examples to validate the potential of all-purpose features for correspondence matching. We adopt DAMv2-small as the LVM encoder, comparing its feature alignment performance with feature extraction of those in stereo or flow estimation algorithms. The max considered disparity is 192 and the metric is Bad 3.0 (%).

ID	Model	Scale	FlyingThings	Middlebury	KITTI 15
0	RAFT [33]		61.9	67.6	58.3
1	LVM (single-layer)	1/8	73.8	79.6	71.8
2	LVM (multi-layers)		65.9	72.5	61.1
0	PSMNet [24]		32.6	66.4	71.0
0	RAFT [33]		32.7	39.1	36.9
1	LVM (single-layer)	1/4	60.8	67.9	57.6
2	LVM (multi-layers)		53.9	62.8	49.0
3	LVM (multi-layers) + Linear		28.2	39.0	24.8

ing. To simplify the analysis, we select 1D displacement estimation (*i.e.*, stereo matching) as a case study and use DAMv2 [77] as the LVM encoder, evaluating its performance in multi-domain scenarios. Specifically, given a stereo image pair, we first extract their all-purpose features using LVM, obtaining HW/p^2 image tokens. Here, p refers to the patch size, H and W denote the height and width of the image, respectively. Next, the resultant image tokens are reshaped to obtain patch-level all-purpose features $F_{l_i} \in \mathbb{R}^{D \times \frac{H}{p} \times \frac{W}{p}}$ with D channels, which undergo bilinear interpolation to achieve high spatial resolution, and then be employed to construct a 3D cost volume using cosine similarity across all disparity levels. Finally, we apply trilinear interpolation to the cost volume to match the input resolution and compute disparity map via $\text{argmax}(\cdot)$ along the disparity dimension (denoted as Model 1). For fair comparison, we implement a baseline (Model 0) using features from either PSMNet [24] or RAFT [33] encoders processed through identical steps without cost aggregation.

To leverage diverse semantic representations, we divide LVM into four segments and collect output tokens of each segment to form multi-layer features. These features are employed to construct four distinct cost volumes, which are then fused through dot product (Model 2). Further-

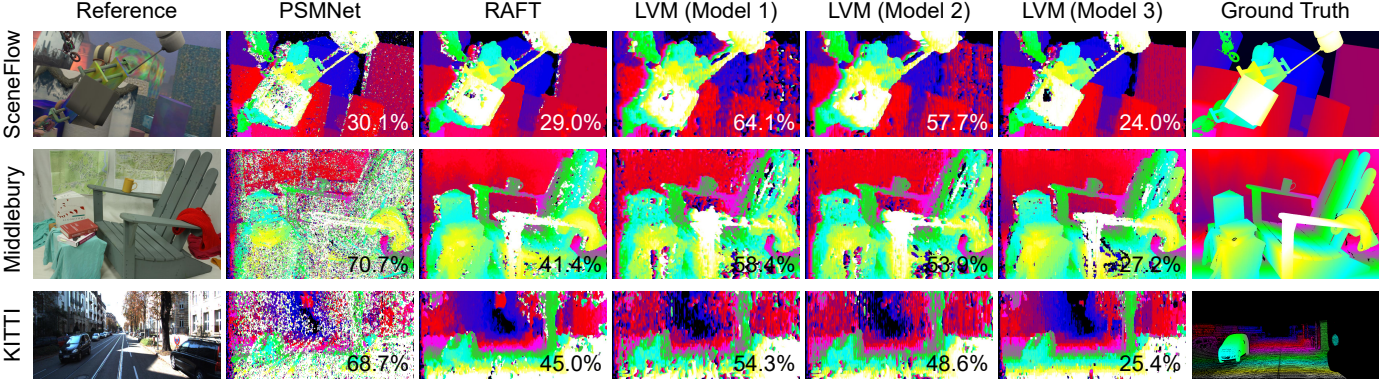


Fig. 4: Disparity estimation from feature matching without cost aggregation. Features extracted by PSMNet [24], RAFT [33], and DAMv2-small [77] are adopted for evaluation. All learnable strategies are only pretrained on the SceneFlow [7] dataset. The metric of Bad 3.0 is reported in each estimation.

more, we replace bilinear interpolation with deconvolution [79] layers, pretraining this variant on FlyingThings [8] for matching-oriented adaptation to improve performance (Model 3).

As quantified in Table 2, all-purpose features demonstrate consistent cross-domain performance. Besides, increasing scales of matching features and utilizing multi-layer features further improve matching accuracy, outperforming the poorly generalized PSMNet on unseen real-world scenes. These observations indicate that comprehensive utilization of all-purpose features provides significant advantages in domain generalization compared to task-specific representations. Furthermore, LVMs combined with simple linear adaptation not only maintain cross-domain consistency but also surpass the well-generalized RAFT in both seen and unseen domains. These findings highlight the potential of all-purpose features for zero-shot matching. Qualitative comparisons in Fig. 4 provide intuitive confirmation that all-purpose features contribute less noisy disparity across domains. Based on these observations, we subsequently employ LVMs as domain-invariant encoders and unleash their potential for matching tasks in the following section.

4.2 General-to-Matching Feature Transformation

We aim to leverage the domain-invariant properties of LVM features to enhance the generalization performance of any selected baseline method. However, directly integrating an LVM with a cost aggregation module produces inferior performance due to mismatches in feature scale, dimension, and pretraining objectives. To address these challenges, we propose a general feature transformation pipeline comprising three core components: (i) a *position-aware guided feature upsampling block* that adaptively interpolates all-purpose features for fine-grained matching while preserving their domain-invariant characteristics; (ii) a *hierarchical adaptation network* that supports multi-layer feature fusion and matching-oriented feature extraction, while accommodating various input formats of cascaded matching baselines; (iii) an explicit *cross-view matching constraint* mechanism that enhances matching-specific attributes within all-purpose features to facilitate task adaptation.

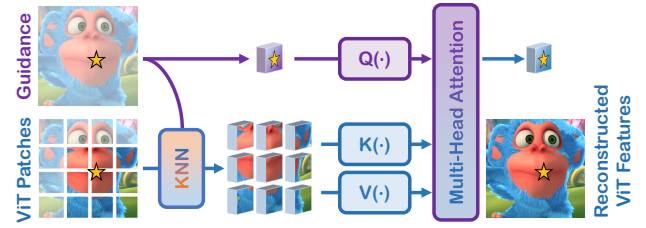


Fig. 5: An overview of the guided feature upsampling block.

4.2.1 Position-Aware Guided Feature Upsampling

Features extracted by LVMs are typically low-resolution, making them insufficient for fine-grained matching. A naïve solution is to apply interpolation to upscale the feature maps. However, existing upsampling strategies typically use fixed, position-independent convolutional kernels ω to obtain s -times high-resolution outputs \mathbf{F}^h from low-resolution inputs \mathbf{F}^l as:

$$\mathbf{F}^h(u, v) = \sum_{i, j} \omega(i, j) \cdot \mathbf{F}^l\left(\frac{u}{s} + i, \frac{v}{s} + j\right), \quad (9)$$

which inherently limits their contextual adaptability and cross-domain generalization.

Instead of directly regressing high-resolution details through static kernels, we propose a position-aware guided feature upsampling strategy, which dynamically adjusts the upsampling kernel weights at different spatial positions during inference. Specifically, we first leverage a lightweight FPN encoder to generate target-resolution guided features, which are treated as the structure-preserving guidance. Then, given an arbitrary position $\mathbf{p} = (u_0, v_0)$ in guidance, as marked by a star in Fig. 5, we project its features into the query space, denoted as $\mathbf{F}_Q^h \in \mathbb{R}^{H \times W \times C}$. Meanwhile, all-purpose features of the correspondent k -nearest neighbors are projected into the key and value spaces, denoted as $\mathbf{F}_K^l \in \mathbb{R}^{h \times w \times C}$ and $\mathbf{F}_V^l \in \mathbb{R}^{h \times w \times C}$, respectively. Here, $H \times W$ represents the target resolution for interpolation, and $h \times w$ means the current size of all-purpose features. Finally, the high-resolution features \mathbf{F}^h at position p are recomposed as:

$$\mathbf{F}^h(\mathbf{p}) = \sum_{\mathbf{q} \in \mathcal{N}(\mathbf{p})} \omega(\mathbf{p}, \mathbf{q}) \cdot \mathbf{F}_V^l(\mathbf{q}), \quad (10)$$

where $\mathbf{q} \in \mathcal{N}(\mathbf{p})$ indicates the 3×3 nearest neighbors of \mathbf{p} in all-purpose features, and $\omega(\mathbf{p}, \mathbf{q})$ denotes the normalized feature similarity scores between query features of pixel \mathbf{p} and key features of pixel \mathbf{q} , *i.e.*,

$$\omega(\mathbf{p}, \mathbf{q}) = \frac{\exp\left(\mathbf{F}_Q^h(\mathbf{p}) \cdot \mathbf{F}_K^l(\mathbf{q}) / \sqrt{C}\right)}{\sum_{\mathbf{q}^* \in \mathcal{N}(\mathbf{p})} \exp\left(\mathbf{F}_Q^h(\mathbf{p}) \cdot \mathbf{F}_K^l(\mathbf{q}^*) / \sqrt{C}\right)}. \quad (11)$$

Note that in Eq. 11, higher similarity scores contribute larger convex combination weights, ensuring that the upsampling process restores sharp edges, contours, and even thin structures, in accordance with the guided features.

Given the similarity between the proposed guided upsampling strategy and the attention mechanism [80], we implement it using an attention-based design and further improve its performance with multi-head attention. To accelerate weight generation through matrix multiplication, we unfold the key and value features using a 3×3 kernel and apply nearest-neighbor interpolation to obtain high-resolution but coarse representations, denoted as $\mathbf{F}_K^h, \mathbf{F}_V^h \in \mathbb{R}^{nHW \times 9 \times (C/n)}$, where n means the number of attention heads. The query features are reshaped as $\mathbf{F}_Q^h \in \mathbb{R}^{nHW \times 1 \times (C/n)}$, and then utilized to construct the upscaled features as:

$$\mathbf{F}^h = \text{Softmax}\left(\mathbf{F}_Q^h \times \left(\mathbf{F}_K^h\right)^T / \sqrt{C/n}\right) \times \mathbf{F}_V^h. \quad (12)$$

Finally, we reshape the features size from $\mathbb{R}^{nHW \times 1 \times (C/n)}$ to $\mathbb{R}^{H \times W \times C}$, and apply an MLP for feature projection.

4.2.2 Hierarchical Adaptation Network

Multi-scale Feature Fusion. Although domain bias has been mitigated by the use of all-purpose features and scale-related issues have been addressed through guided upsampling, simply grafting matching baselines with LVMs remains suboptimal. This limitation arises because LVMs are not pretrained for correspondence matching. As a result, the all-purpose features may not align with the task of accurate correspondence matching.

To remedy the aforementioned issue, we propose a U-shaped fusion adapter. Specifically, we first employ a multi-stage CNN encoder to generate multi-scale guidance features. Meanwhile, we collect multi-layer all-purpose features from several segments of LVM, establishing a one-to-one correspondence with the multi-scale CNN features. Next, we construct multi-scale all-purpose features via guided upsampling blocks, wherein each scale-specific feature map is recomposed by upsampling the corresponding all-purpose features under the guidance of target-scale CNN features. We then employ ConvNeXt blocks [81] to construct the standard feature pyramid decoder, resulting in feature pyramid at resolutions of $1/16$, $1/8$, $1/4$, and $1/2$ relative to the original image size.

Multi-scale Patch Embedding. U-Net progressively aggregates multi-scale features ranging from $1/16$ to $1/2$ resolution. However, most methods build cost volumes only at the $1/8$ scale, neglecting the richer details captured at $1/4$ and $1/2$ resolutions. To address this limitation, we propose a multi-scale patch embedding block to effectively fuse features from multiple scales into a unified target feature

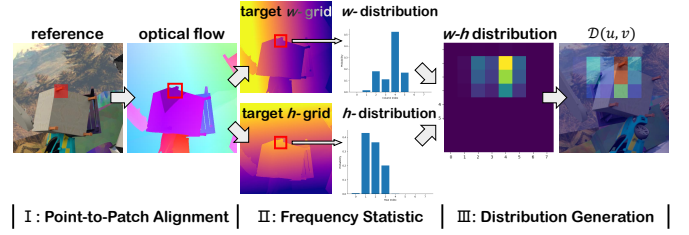


Fig. 6: A pipeline to obtain the patch correspondence distribution from ground-truth optical flow map.

space at one step. Specifically, we use patch sizes of 4, 2, 1, and $1/2$ to fold the feature maps at scales of $1/2$, $1/4$, $1/8$, and $1/16$, respectively. This design ensures that all scales features are position-aligned with the $1/8$ scale one. Subsequently, we apply four independent linear projections to compress and transform features at each scale, which are then concatenated along the feature dimension. Finally, a multi-layer perceptron (MLP) is used to generate the fused features at the target scale.

4.2.3 Cross-View Matching Constraint

The parameterized feature transformation and projection only account for the single-view constraints, overlooking the extraction of cross-view consistent representations. Although the displacement supervision [8], [33] provides implicit guidance for aligning cross-view representations at matching points, it places only weak constraints on unrelated proposals, raising the risks of multi-modal distribution and ultimately degrades the quality of the regression results, as demonstrated in Fig. 15. To emphasize the importance of learning cross-view consistent representations, we leverage contrastive learning for enhancing the feature similarity on the correspondences while impress on the other regions.

Specifically, given paired features $\{\mathbf{F}_{ref}, \mathbf{F}_{tar}\}$, we first normalize these representations along feature dimension and then calculate the cosine similarity of normalized feature pairs under each flow proposal to obtain the 3D score volume $\mathbf{S} \in \mathbb{R}^{h \times w \times hw}$ as:

$$\mathbf{S}(u, v, \mathbf{f}) = \sum_c \mathbf{F}_{ref}(u, v) \cdot \mathbf{F}_{tar}(u + \mathbf{f}_u, v + \mathbf{f}_v). \quad (13)$$

To ensure that the score volume is provided with similarity prior, we apply a pixel-wise infoNCE [82] loss to the 3D score volume, increasing the proportion of matching pixel score among all candidates so that easier to distinguish correspondences among proposals. This is formulated as:

$$\mathcal{L}_{NCE}(u, v) = \sum_{\mathbf{f}} -p(u, v, \mathbf{f}) \cdot \log \frac{\exp(\mathbf{S}(u, v, \mathbf{f})/\tau)}{\sum_{\mathbf{f}'} \exp(\mathbf{S}(u, v, \mathbf{f}')/\tau)}, \quad (14)$$

where $p(u, v, \mathbf{f})$ indicates the probability of proposal \mathbf{f} in the ground-truth discrete distribution $\mathcal{D}(u, v)$, τ is a temperature coefficient and we set $\tau = 0.07$ following [40]. The ground-truth discrete distribution $\mathcal{D}(u, v)$ is derived from ground-truth optical flow map, as illustrated in Fig. 6. Specifically, we first compute the target coordinates within the reference coordinate system using the ground-truth optical flow. Due to the resolution discrepancy between the feature map and the coordinate map, each feature point corresponds to a small patch on the coordinate maps. We

TABLE 3: Datasets used for training PanMatch. Datasets used for fine-tuning are highlighted in boldface.

Dataset	Annotation	Scene Type	Frames	Image Size
FlyingChairs [8]	Optical Flow	Synthetic	~23k	384x512
FlyingThings [7]		Synthetic	~81k	540x960
Monkaa [7]		Outdoors	~35k	540x960
AutoFlow [9]		Synthetic	~27k	448x576
Dynamic Replica [83]		Indoors	~144k	720x1280
Tartanair [11]	Depth	Outdoors	~306k	480x640
Kubric [55]		Synthetic	~132k	512x512
CVO [84]		Synthetic	~125k	512x512
VirtualKITTI2 [10]	Disparity	Driving	~42k	375x1242
Hypersim [12]		Indoors	~367k	768x1024
MegaDepth [13]		Outdoors	~285k	480x640
CRIStereo [5]		Synthetic	~200k	1080x1920
FallingThings [6]		Indoors	~62k	540x960

therefore quantize the coordinates within each patch to obtain frequency counts along both horizontal and vertical axes. Finally, the ground-truth flow distribution is generated from the joint distribution of these horizontal and vertical frequencies.

Note that we set $\mathcal{L}_{NCE} = \text{mean}(\sum_{u,v} \mathcal{L}_{NCE}(u,v))$ and intentionally do not exclude occluded regions, even though cosine similarity may not yield meaningful metrics there, as we aim to ensure that the output features exhibit global representational capabilities and respond appropriately to occluded areas.

4.3 Loss Function

We supervise our network using loss \mathcal{L}_{disp} , which follows the same formulation as the adopted baseline and measures the distance between the predicted and ground-truth displacements over the full sequence of predictions. In addition, we incorporate a contrastive learning loss \mathcal{L}_{NCE} to promote the learning of cross-view consistent representations in the adopter module. The complete loss function is defined as

$$\mathcal{L} = \mathcal{L}_{disp} + \mathcal{L}_{NCE}. \quad (15)$$

5 EXPERIMENTS

In this section, we first describe the development of PanMatch in Secs. 5.1, then compare it with both unified correspondence methods and task-specific methods in Sec. 5.2 and Sec. 5.3 respectively, highlighting its versatile performance across multiple benchmarks. Next, we conduct an ablation study to assess our contributions in Sec. 5.4. Finally, we present the advantages of our unified models over independent methods for real-world application in Sec. 5.5.

5.1 Implementation Details

5.1.1 Training Datasets

Unlike previous methods that are pretrained on small-scale datasets [7], [8], [51], we emphasize the importance of data diversity and collect a broad range of available optical flow datasets. Additionally, we incorporate datasets from feature matching and stereo matching tasks to further enrich the diversity of training samples. The annotations are obtained by converting ground-truth depth or disparity maps using camera parameters, as illustrated in Fig. 7. The datasets adopted in our experiments are summarized in Table 3.

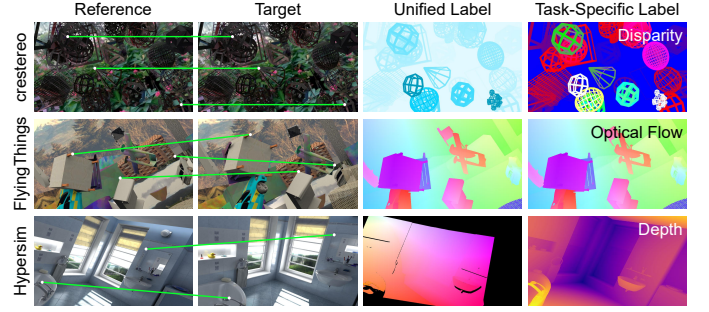


Fig. 7: Diversity of the training data. Each row shows paired inputs in the first two columns with a few correspondences marked to illustrate their characteristics. The corresponding ground-truth displacement in the third column is derived from the dataset’s original annotations in the fourth column.

5.1.2 Training Strategies

We use DINOv2-reg-giant [66], [85] as the LVM encoder and select FlowFormer [50] as the cross-view aggregation baseline to construct PanMatch. We employ a three-stage training strategy during the training phase.

- Stage 1: We follow the training protocol in [50] to establish a common optical flow baseline. Images are randomly cropped to a size of 448×448 .
- Stage 2: The datasets listed in Table 3 are included to train our PanMatch for 300k iterations with a batch size of 8. We keep the randomly cropped image to a size of 448×448 unchanged.
- Stage 3: Only datasets shown in boldface in Table 3 are included to fine-tune our PanMatch for 60k iterations. Specifically, the cropped image size is increased to 672×896 .

The core idea of our three-stage training strategy is to progressively learn displacement distributions, which starts from a single task, then moves to multiple tasks, and finally culminates in challenging fine-grained multi-task scenarios. Throughout all three stages, we use the AdamW [86] optimizer and the one-cycle learning rate schedule, with the maximum learning rate being set to 1×10^{-4} . Data augmentations including color jitter, asymmetric occlusion and image flipping [33] are conducted during training. For stereo pairs, we randomly shift the right-view cropping window in the vertical direction, alleviating distribution imbalance caused by abundant zero displacement in stereo-based datasets. Besides, we randomly rotate the cropped stereo pair to interchange horizontal and vertical displacement components, promoting equitable training of both components. For posed images captured in rigid scenes [12], [13], we select adjacent poses with similar perspectives as posed pairs and convert their depth according to Eq. 4 to obtain the corresponding displacement annotations for the same observation area, as illustrated in the 3rd row of Fig. 7.

5.2 Comparison with Unified Models

5.2.1 Baselines

With our unified formulation, existing optical flow estimation algorithms can be extended to unified matching

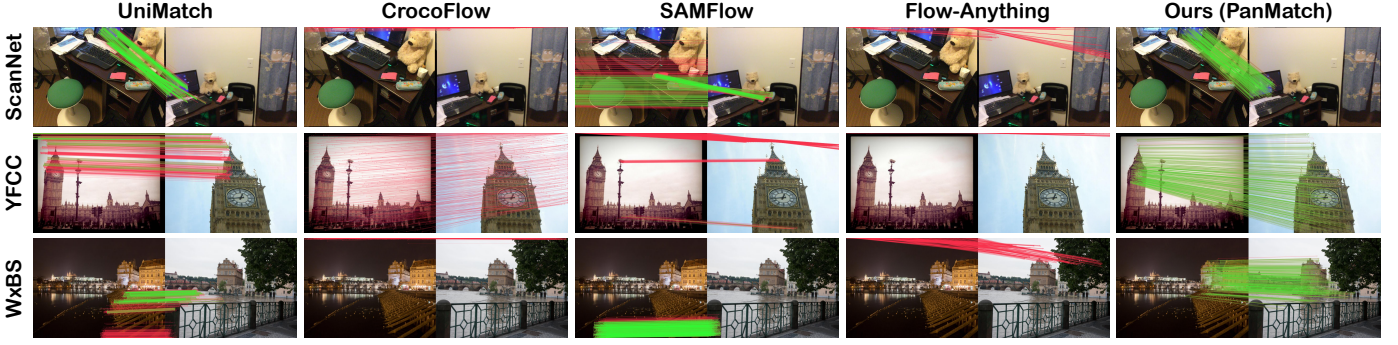


Fig. 8: Qualitative results on the ScanNet [92], YFCC [93], and WxBS [94] datasets. All methods employ the same outlier filtering method and confidence threshold.

models that support diverse outputs across multiple tasks. Consequently, we select four state-of-the-art optical flow algorithms for evaluation, including UniMatch [1], CrocoFlow [14], SAMFlow [78] and Flow-Anything [87]. Note that, both CrocoFlow and Flow-Anything employ million-scale datasets for self-supervised pretraining, while SAMFlow [78] leverages SAM [71] to enhance the accuracy of the estimated optical flow.

5.2.2 Benchmarks and Metrics

We select three tasks (including stereo matching, optical flow estimation and feature matching) to evaluate the performance of unified models in static scenes, dynamic scenes, and geometrically varying scenes, respectively. For stereo matching, we assess disparity accuracy on the Middlebury (train-h) [88], ETH3D (train) [89], and KITTI 2012 (train) [54] datasets. We use percentage of accuracy in threshold x pixel (PCA x) as the evaluation metric, setting threshold 1px for ETH3D, 2px for Middlebury and 3px for KITTI, respectively. For optical flow, benchmarks including Infinigen [90] and Spring [91] are employed, with PCA 1 being employed for evaluation. For feature matching, we assess pose estimation accuracy on the ScanNet-1500 [92] and YFCC100M [93] datasets, and eigenvector estimation accuracy on the WxBS [94] dataset. Before feature matching evaluation, we employ a forward-backward circular consistency check to filter out correspondence outliers.

5.2.3 Multi-Task Evaluation

Optical Flow Estimation. As illustrated in Fig. 9, our approach achieves the highest accuracy on both the Infinigen and Spring validation dataset. Specifically, PanMatch attains 0.32 EPE on Infinigen and 0.31 EPE on Spring, leading 16% and 23% reductions compared to the second-best method (i.e., 0.38 EPE on Infinigen and 0.40 EPE on Spring).

Stereo Matching. Our approach outperforms the second best competitor by 30%, 16%, and 10% on the Middlebury, ETH3D, and KITTI12 datasets, respectively, underscoring its superior cross-task transferability. To facilitate an intuitive comparison, we present disparity estimates from an ETH3D test scene in Fig. 10. As illustrated, existing flow-based methods falter on complex, overlapping structures, yielding ambiguous foreground-background boundaries and blurred object contours, which impair disparity accuracy. In contrast, our method precisely delineates fine details and

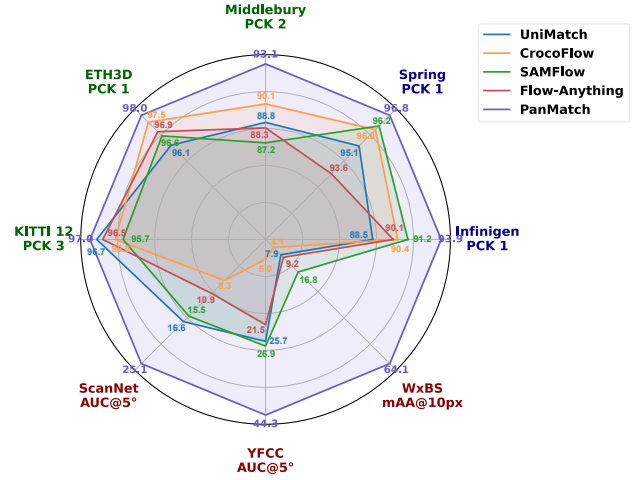


Fig. 9: Zero-shot comparison on multiple domains and tasks, including optical flow estimation, stereo matching and feature matching.

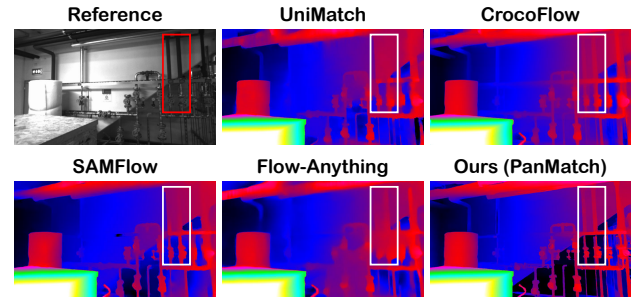


Fig. 10: Comparison on an ETH test scene. Zoom out for better view.

preserves subtle disparity variations.

Feature Matching. As illustrated in Fig. 9, existing flow-based methods struggle to perform feature matching tasks directly, exhibiting low performance compared to our approach. We provide a qualitative comparison in Fig. 8 for discussion. It can be observed that input pairs sampled from the ScanNet dataset exhibit large inter-frame motions and significant viewpoint changes, which limits the correspondence estimation accuracy for methods like CrocoFlow and Flow-Anything. Similarly, on the YFCC and WxBS datasets, drastic variations in appearance and pose yield

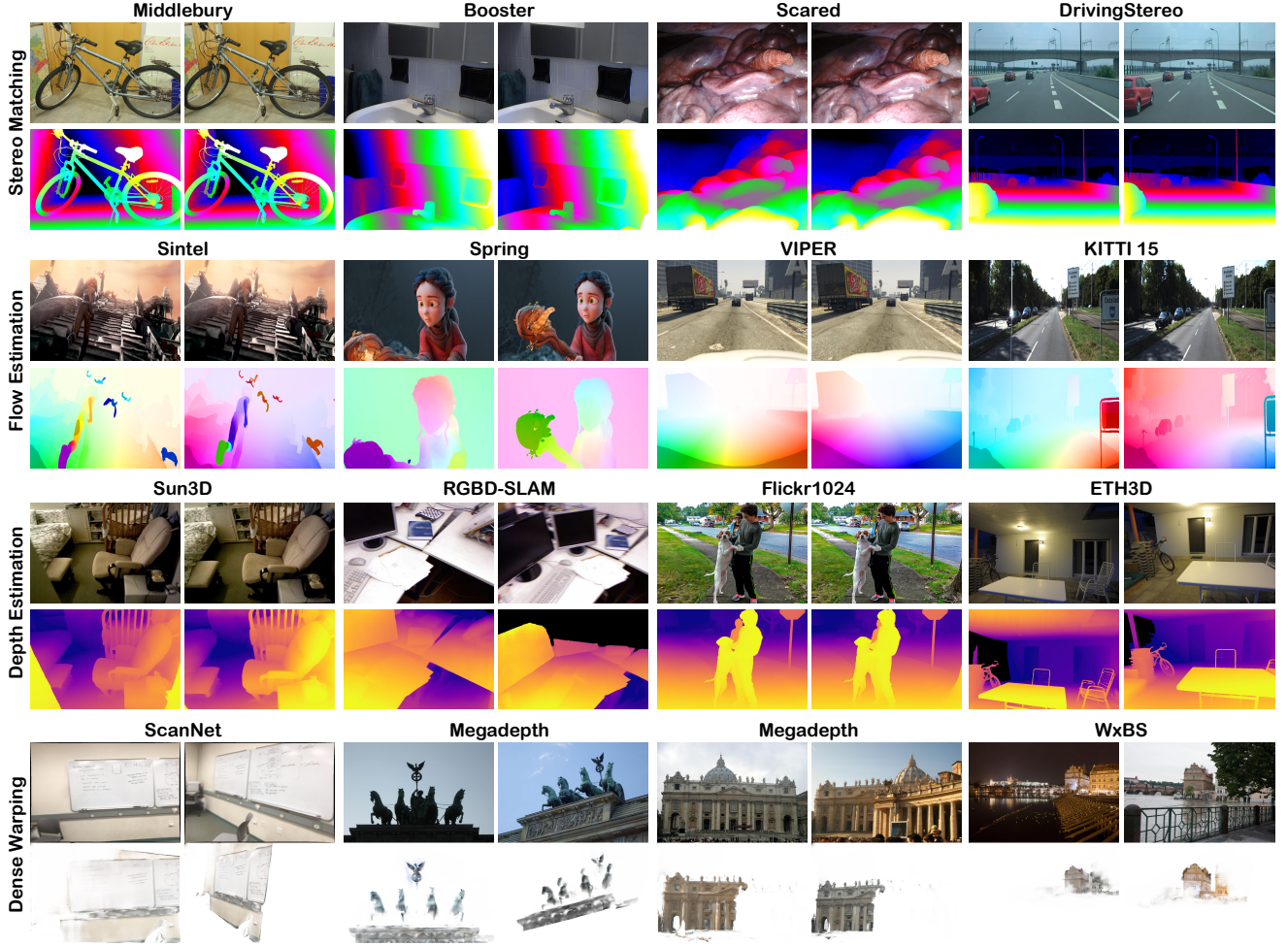


Fig. 11: The versatile performance of PanMatch on a wide range of tasks and datasets [13], [51], [52], [53], [88], [89], [91], [92], [94], [95], [96], [97], [98], [99], [100]. Given a pair of two-view input, PanMatch can output disparity (group in the 1st row), optical flow (group in the 2nd row), relative depth (group in the 3rd row) and dense warping correspondences (group in the 4th row). Note that all test scenes are never seen during training.

few usable matches for all competing methods, severely impairing downstream tasks like pose and essential matrix estimation. In contrast, our approach remains robust under these challenging conditions, achieving significant performance gains against other methods.

Qualitative Evaluation. We have visualized the zero-shot capability and multi-task versatility of our unified model on a broader range of tasks and datasets. As shown in Fig. 11, our model can obtain reasonable outputs after a single feed-forward inference.

5.3 Comparison with Task-Specific Models

5.3.1 Stereo Matching and Optical Flow

Zero-shot Comparison. We evaluate zero-shot stereo matching performance on the half- and quarter-resolution subsets of Middlebury, the 2015 and 2012 training splits of KITTI, and the ETH3D training set. Evaluation metrics include non-occluded Bad 2.0 for Middlebury, non-occluded Bad 1.0 for ETH3D, and D1-all for KITTI. We compare our method to state-of-the-art generalized stereo matching algorithms, as well as optical flow models fine-tuned on multiple real-world datasets. As shown in Table 4, RVC models [1], [101]

fine-tuned on real-world data significantly outperform those generalizable variants of PSMNet and RAFT-Stereo, indicating that pretraining on diverse data substantially improves cross-domain robustness. Furthermore, by pretraining on a large-scale, high-quality mixture of synthetic datasets, our PanMatch achieves the lowest zero-shot errors across all benchmarks, significantly outperforming FlowFormer++ and CrocoFlow that are pretrained on larger-scale but unlabeled data. These comparisons underscore the importance of both the scale and quality of pretraining data.

For zero-shot optical flow estimation, we evaluate on the training subsets of Sintel and KITTI-Flow. Table 5 similarly shows that methods pretrained with additional data exhibit lower generalization errors, with our approach achieving the best results thanks to its use of large-scale annotated pairs.

Note that our feature transformation pipeline can be seamlessly integrated into existing backbones, such as PSMNet, RAFT, and FlowFormer, by replacing their native feature extractors. We further validate its ability to enhance generalization when pretraining data are restricted. As highlighted by the colored cells in Table 4 and 5, integrating

TABLE 4: Zero-shot comparison on stereo matching task. † means testing on the training data.

Extra Data	Method	Middlebury		KITTI		ETH3D
		Half	Quarter	2015	2012	
	PSMNet [24]	26.9	20.0	16.3	15.1	23.8
	MS-PSMNet [38]	19.8	10.8	7.8	14.0	16.8
	FC-PSMNet [40]	15.1	9.3	5.8	5.3	9.5
	ITSA-PSMNet [4]	12.7	9.6	5.8	5.2	9.8
	Graft-PSMNet [39]	9.7	-	4.8	4.3	7.7
	HVT-PSMNet [42]	10.2	-	4.9	4.3	6.9
	HODC-PSMNet [102]	9.3	7.0	4.7	3.9	5.4
	ADL-PSMNet [103]	8.9	-	4.8	4.2	3.4
	Former-PSMNet [17]	7.7	6.2	5.0	3.9	6.7
	Ours+PSMNet	7.63	5.20	4.68	3.06	5.09
	RAFT-Stereo [34]	12.6	-	5.7	5.1	3.3
	HVT-RAFT [42]	10.4	-	5.2	3.7	3.0
	Former-RAFT [17]	8.1	5.4	5.1	3.9	3.3
S+V+H+KITTI	GMFlow_RVC [1]	6.83	6.04	2.92†	3.13†	3.27
	MS_RAFT+_RVC [101]	7.15	6.20	2.00†	2.58†	5.10
YouTube-VOS	FlowFormer++ [104]	10.99	10.21	6.12	4.50	4.63
CroCo-Pretrain	CrocoFlow [14]	7.08	-	4.19	3.83	2.59
Table 3	PanMatch	3.39	3.64	3.27	2.77	1.79

TABLE 5: Zero-shot evaluation on optical flow estimation task. All models are pretrained with C+T scheduler.

Extra Data	Method	Sintel		KITTI	
		Clean	Final	F1-epe	F1-all
	PWC-Net [45]	2.55	3.93	10.4	33.7
	RAFT [33]	1.43	2.71	5.04	17.4
	GMA [47]	1.30	2.74	4.69	17.1
	SKFlow [105]	1.22	2.46	4.27	15.5
	SEA-RAFT [48]	1.19	4.11	3.62	12.9
	GMFlow [49]	1.08	2.48	-	-
	CCMR+ [106]	0.98	2.36	-	12.8
	FlowFormer [50]	0.94	2.33	4.09	14.7
	SAMFlow [78]	0.87	2.11	3.44	12.3
	Ours+RAFT	1.27	2.29	3.76	12.58
	Ours+FlowFormer	0.83	2.05	3.10	12.12
MegaDepth	MatchFlow(G) [107]	1.03	2.45	4.08	15.6
YouTube-VOS	FlowFormer++ [104]	0.90	2.30	3.93	14.1
CroCo-Pretrain	CrocoFlow [14]	-	-	3.39	10.3
M+T+S	RGM [2]	0.90	2.40	3.90	12.5
Table 3	PanMatch	0.85	1.67	1.94	5.54

this module boosts generalization, yielding at least a 70% generalization gain for PSMNet, 11% for RAFT and 12% for FlowFormer. Notably, our integrated PSMNet outperforms other generalizable PSMNet variants under the same settings, underscoring the effectiveness of our architecture for robust generalization.

Robust Vision Challenges. Consistent with the objectives of this study, recent Robust Vision Challenges (RVC) aim at achieving robust performance across multiple benchmarks using a single model checkpoint. These approaches typically leverage multiple synthetic datasets for pretraining and various benchmark datasets for fine-tuning, thus significantly advancing real-world applications. To evaluate the performance of PanMatch against these robust models, we submit its evaluation results to benchmarks and report the latest RVC leaderboard rankings for stereo matching and optical flow tasks in Table 6 and Table 7, respectively. Note that PanMatch has neither been trained nor fine-tuned on any benchmark-related data, which is unlike competing methods that inherently benefit from such data to boost accuracy. Nevertheless, PanMatch still outperforms most task-specific approaches. Our PanMatch achieves the best performance on the ETH3D and Spring benchmark,

while exhibits comparable performance on the Middlebury and Sintel benchmarks. We hypothesize that the limited amount of 27 ETH3D training samples is insufficient for RVC methods to model in-domain characteristics. Consequently, model accuracy on this benchmark is dominated by zero-shot performance. In contrast, KITTI, Middlebury and Sintel offer relatively abundant training data, allowing RVC methods to fit in-domain characteristics effectively and outperform our zero-shot model on these seen datasets.

We argue that not ranking first on benchmark leaderboards does not necessarily indicate inferior real-world performance compared to task-specific methods fine-tuned with real-world datasets, as existing benchmarks do not fully represent real-world scenarios. Indeed, there exist challenging scenes where current RVC methods clearly lack robustness. Specifically, we select the top 2 open-sources methods from the RVC stereo and optical flow leaderboard, *i.e.*, iRaftStereo_RVC [34], [111], CFNet_RVC [109], GMFlow_RVC [1], MS-RAFT+_RVC [101], as well as the recent LoS_RVC [113], and evaluate their performance on the Booster [95], [116] dataset. Booster is an indoor dataset characterized by diverse lighting conditions and challenging non-Lambertian materials such as mirrors and transparent windows. We quantitatively evaluate all methods on the Booster dataset at quarter resolution (*i.e.*, 1028×752) in Table 8, whose results indicating that these RVC methods struggle on previously unseen scenes and consequently lose their advantage over PanMatch. Qualitative comparisons in Fig. 12 further reveal that in challenging scenarios such as rainy day [97], dark streets [117], and satellite imagery [118], existing RVC algorithms fail to produce reliable results, whereas PanMatch consistently yields robust estimations.

5.3.2 Feature Matching

We evaluate PanMatch on widely adopted feature matching benchmarks, including ScanNet-1500 [92], MegaDepth-1500 [13], and WxBS [94]. Following the evaluation in RoMa [63], we assess pose estimation accuracy on ScanNet and MegaDepth, and compute the mean average accuracy (mAA) on ground truth correspondences consistent with the estimated fundamental matrix at a 10-pixel threshold for WxBS. To obtain reliable confidence estimation for PanMatch, we employ forward-backward cycle consistency in flow estimation to obtain the final confidence map. Results are presented in Table 9, which indicate that PanMatch achieves comparable performance on ScanNet even without fine-tuning on the specific indoor feature matching dataset. Besides, PanMatch outperforms most feature matching algorithms on the difficult WxBS benchmark and achieves the second best performance. This is highly exciting since PanMatch is neither explicitly pretrained on the feature matching task nor designed to optimize correspondence selection for pose estimation [63], [64].

5.3.3 Depth Estimation

As demonstrated in Sec. 3.2, our unified model can output metric depth from the estimated flow once the camera parameters are available. To evaluate the depth estimation accuracy of PanMatch, we test it on four depth benchmarks, including RGBD-SLAM [99], Sun3D [98], Scenes11 [120] and ScanNet [92]. Following unrectified two-view depth

TABLE 6: Robust vision challenges on stereo matching benchmarks.

Method	Middlebury				KITTI 2015				ETH3D			
	bad 2.0 (%)	bad 4.0 (%)	AvgErr	Rank	D1-bg (%)	D1-fg (%)	D1-All (%)	Rank	bad 1.0 (%)	bad 2.0 (%)	AvgErr	Rank
AANet_RVC [26]	31.8	25.8	12.8	13	2.23	4.89	2.67	11	5.41	1.95	0.33	11
GANet_RVC [25]	24.9	16.3	15.8	12	1.88	4.58	2.33	9	6.97	1.25	0.45	13
HSMNet_RVC [29]	16.5	9.68	3.44	6	2.74	8.73	3.74	13	4.40	1.51	0.28	10
MaskLacGwcNet_RVC [43]	15.8	10.3	13.5	9	1.65	3.68	1.99	7	6.42	1.88	0.38	12
NLCANetV2_RVC [108]	16.4	10.3	5.60	8	1.51	3.97	1.92	5	4.11	1.20	0.29	9
Croco_RVC [14]	19.7	12.2	5.14	11	2.04	3.75	2.33	10	1.54	0.50	0.21	5
CFNet_RVC [109]	16.1	11.3	5.07	7	1.65	3.53	1.96	6	3.70	0.97	0.26	8
UCFNet_RVC [110]	16.7	10.9	5.96	10	1.57	3.33	1.86	3	3.37	0.78	0.25	7
iRaftStereo_RVC [111]	13.3	8.02	2.90	5	1.88	3.03	2.07	8	1.88	0.55	0.17	6
CREStereo++_RVC [112]	9.46	6.25	2.20	4	1.55	3.53	1.88	4	1.70	0.37	0.16	4
LoS_RVC [113]	9.30	6.03	2.36	3	1.58	3.03	1.83	2	1.47	0.25	0.14	3
DEFOM-Stereo_RVC [114]	6.90	4.25	1.61	1	1.42	2.68	1.63	1	1.09	0.26	0.13	2
PanMatch (Zero-shot)	11.4	5.71	1.78	2	2.74	6.26	3.33	12	0.61	0.14	0.15	1

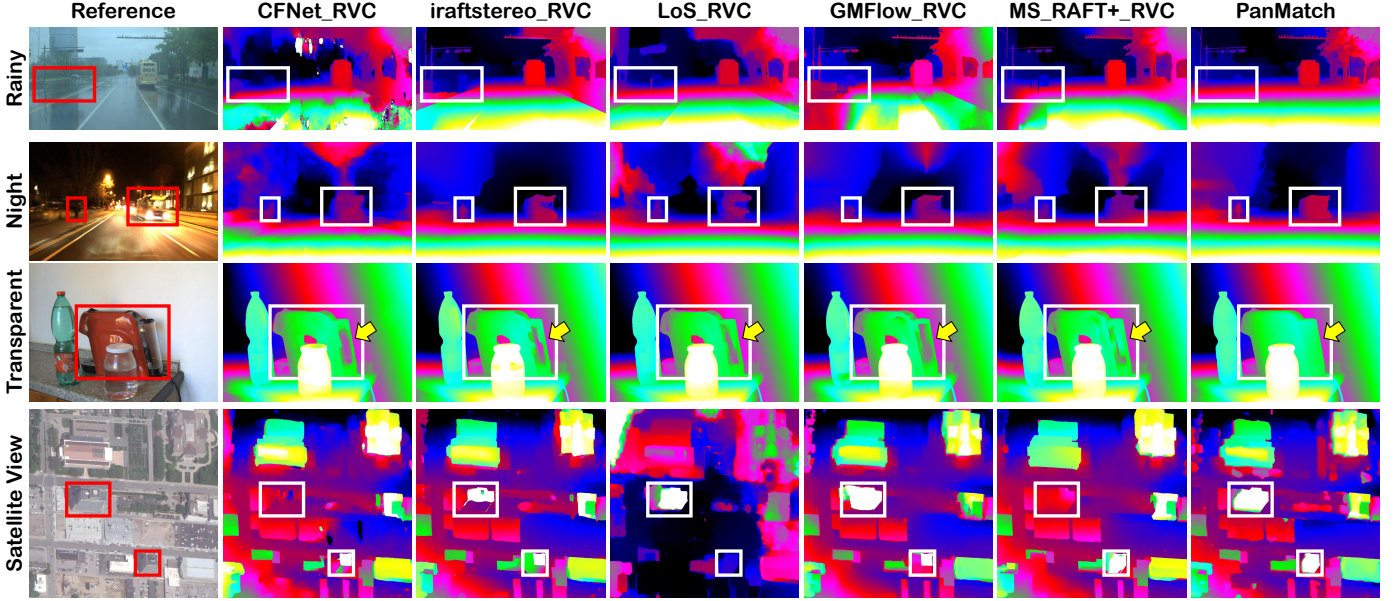


Fig. 12: The real-world zero-shot capacity between RVC algorithms and our proposed PanMatch tested on four abnormal scenes, including rainy day of DrivingStereo [97], night time of Oxford Robot Car [117], transparent object in Booster [95] and satellite scene in UrbanSemantic3D [118]. Challenging regions are marked by the white boxes. Zoom out for better view.

TABLE 7: RVC comparison on optical flow benchmarks.

Method	KITTI F1-All	Spring Bad 1.0	Sintel	
			Clean	Final
RAFT-TF_RVC [33]	5.56	-	1.187	3.321
GMFlow_RVC [11]	4.41	-	1.055	2.218
RAFT-it+_RVC [115]	3.90	-	1.837	2.696
MS_RAFT+_RVC [101]	4.15	5.724	1.232	2.682
PanMatch (Zero-shot)	5.64	4.221	1.073	2.481

TABLE 8: Zero-shot comparison on Booster training set.

Method	Type	Metric			
		EPE	bad 2.0	bad 3.0	bad 5.0
CFNet_RVC [109]	Stereo	4.72	17.51	14.58	12.01
iRaftStereo_RVC [34]		4.01	13.21	11.17	9.47
LoS_RVC [113]		2.36	10.74	8.54	6.93
GMFlow_RVC [1]	Flow	3.78	26.88	16.39	11.10
MS_RAFT+_RVC [101]		4.14	21.34	13.85	10.57
PanMatch		1.95	17.45	6.82	4.20

estimation methods, we use four error metrics to assess depth quality, including absolute relative difference (Abs Rel), squared relative difference (Sq Rel), root mean squared

TABLE 9: Comparisons on feature matching benchmarks. Higher metrics means better performance. [†] means the model only uses forward-backward circle consistency as the confidence map.

Method	ScanNet-1500			Megadepth-1500			WxBS mAA@10
	AUC@5	10	20	AUC@5	10	20	
LoFTR [62]	22.1	40.8	57.6	52.8	69.2	81.2	55.4
PDC-Net+ [69]	20.3	39.4	57.1	51.5	67.2	78.5	-
ASpanFormer [119]	25.6	46.0	63.3	55.3	71.5	83.1	-
DKM [64]	29.4	50.7	68.3	60.4	74.9	85.1	58.9
RoMa [63]	31.8	53.4	70.9	62.6	76.7	86.3	80.1
PanMatch [†]	25.1	44.8	61.5	50.9	66.8	78.9	64.2

error (RMSE) and RMSE in log scale (RMSE log). As shown in Table 10, PanMatch achieves comparable performance across most metrics, and outperforms existing methods in terms of Sq Rel across four datasets, despite not being fine-tuned for the depth regression task. These results highlight the effectiveness and practicality of displacement-based depth estimation, and demonstrate the strong cross-task generalization capacity of PanMatch.

TABLE 10: Depth estimation results.

Dataset	Method	Abs Rel	Sq Rel	RMSE	RMSE log
RGBD-SLAM	DeMoN [120]	0.157	0.524	1.780	0.202
	DeepMVS [121]	0.294	0.430	0.868	0.351
	DPSNet [122]	0.154	0.215	0.723	0.226
	IIB [123]	0.095	-	0.550	-
	GMDepth [1]	0.101	0.177	0.556	0.167
	PanMatch	0.123	0.134	0.568	0.190
SUN3D	DeMoN [120]	0.214	1.120	2.421	0.206
	DeepMVS [121]	0.282	0.435	0.944	0.363
	DPSNet [122]	0.147	0.107	0.427	0.191
	IIB [123]	0.099	-	0.293	-
	GMDepth [1]	0.122	0.068	0.336	0.146
	PanMatch	0.106	0.063	0.311	0.150
Scenes11	DeMoN [120]	0.556	3.402	2.603	0.391
	DeepMVS [121]	0.210	0.373	0.891	0.270
	DPSNet [122]	0.056	0.144	0.714	0.140
	IIB [123]	0.056	-	0.523	-
	GMDepth [1]	0.050	0.069	0.491	0.106
	PanMatch	0.031	0.029	0.307	0.083
ScanNet	DeMoN [120]	0.231	0.520	0.761	0.289
	GMDepth [1]	0.059	0.019	0.169	0.080
	PanMatch	0.064	0.019	0.148	0.090

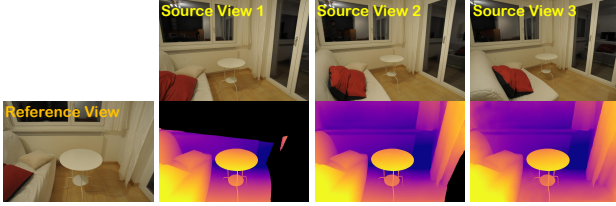


Fig. 13: Two-view depth estimation. Each result comes from the same reference image and adjacent source inputs. Slightly changing the camera pose can find a suitable view-point to obtain a complete depth estimation map.

Note that we only assess the valid regions of each estimated depth map since our model may output a semi-dense depth map after depth validity check, which is adopted to filter potential numerical issues caused by division by zero in Eq. 5 or Eq. 6. Such situations occur when camera motion exhibits zero translation or is purely along the optical axis. This does not point a weakness, as the semi-density issues can be easily alleviated by slightly adjusting the camera pose, which is practically achievable as illustrated in Fig. 13. Additionally, we highlight the strong zero-shot generalization advantage of PanMatch, which makes it more suitable for real-world applications. Furthermore, since PanMatch can estimate the relative pose from reliable correspondences, it reduces the need for prior pose information, showing strong convenience for depth estimation in real-world scenarios compared to unrectified two-view algorithms.

5.4 Model Analyses

5.4.1 Ablation Study

We conduct experiments to validate the contributions of each block designed in the feature transformation pipeline. For simplicity, all ablation study defaultly use DAMv2-Base as the LVM encoder, and FlowFormer as the cross-matching baseline. We using C+T training scheduler [45] and approximately assess the real-world generalization ability by evaluating these variants on the training sets of the Sintel, KITTI and Middlebury datasets.

TABLE 11: Ablation study on interpolation strategy.

Interpolation	Sintel clean	Sintel final	KITTI EPE	Middlebury Bad 2.0
Bilinear	1.05	2.26	4.48	14.89
Deconvolution	1.02	2.10	3.83	12.83
Pixel shuffling	0.95	2.12	3.39	11.29
Ours	0.89	2.07	3.37	10.86

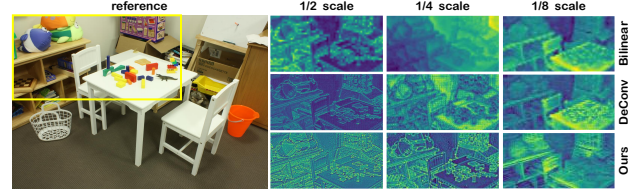


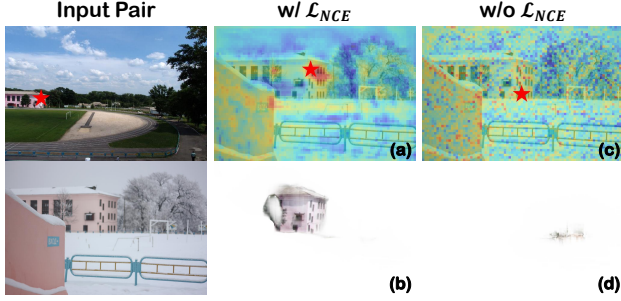
Fig. 14: PCA analysis.

Guided Feature Upsampling. In PanMatch, we propose a guided feature upsampling block to recompose feature maps at arbitrary scales under appropriate guidance. This module can be replaced by standard interpolation methods, such as bilinear interpolation, deconvolution, or pixel shuffling, once the target scale is known. We constructed network variants employing these interpolation methods, investigating the necessity and effectiveness of the proposed block. As shown in Table 11, our proposed block achieves the best generalization performance on the Sintel, KITTI and Middlebury datasets. To investigate what causes the differences among these upsampling strategies in terms of domain generalization, we present Principal Component Analysis (PCA) visualizations along the channel dimension of the upsampled features for intuitive comparison. As illustrated in Fig. 14, bilinear interpolation fails to recover detailed information such as edges and small objects in the feature maps, resulting in increasingly blurry features as the required scale grows. Although deconvolution generates sharp contours in high-resolution features, it also introduces checkerboard artifacts, particularly in textureless regions. These artifacts can lead to multi-modal matching distributions and hinder accurate target regression. In contrast, our proposed guided feature upsampling method restores scene details and semantics with clear representations across scales, demonstrating strong generalization capabilities and ultimately enabling precise 2D displacement estimation.

Network Design and Auxiliary Losses. The proposed adapter employs a shallow Feature Pyramid Network (FPN) to facilitate task-specific adaptation and multi-scale feature fusion. Subsequently, Multi-scale Patch Embedding (MPE) integrates these multi-scale features into unified representations, which are ultimately supervised using an InfoNCE loss \mathcal{L}_{NCE} . To systematically evaluate the contributions of each component toward model generalization, we first establish a baseline model composed of the LVM encoder, a guided upsampling module, and a cross-matching algorithm. Then, we incrementally introduce the FPN, MPE, and \mathcal{L}_{NCE} . As demonstrated in Table 12, progressively incorporating these components significantly enhances the model's generalization performance across multiple datasets. Specifically, introducing FPN and MPE enables the model to effectively utilize information from multiple layers of the ViT

TABLE 12: Ablation study on module design. Lower is better.

FPN	MEP	\mathcal{L}_{NCE}	Sintel clean	Sintel final	KITTI F1-All	Middlebury Bad 2.0
✗	✗	✗	1.08	2.11	13.93	15.09
✓	✗	✗	1.04	2.05	13.73	14.86
✓	✓	✗	0.89	2.07	12.41	10.86
✓	✓	✓	0.83	2.05	12.12	10.04

Fig. 15: Generalization enhancement by \mathcal{L}_{NCE} . Here, Figs. (a) and (c) are heatmaps generated by feature matching, and (b) and (d) are warped images from another view.

encoder, substantially improving both estimation accuracy and generalization capability. These findings align with the conclusions drawn from the toy experiments in Sec. 4.1. Additionally, the integration of the InfoNCE loss enhances the discriminative capability of the representations utilized to construct the cost volume, thereby improving the model’s generalization. This hypothesis is validated in Fig. 15, which visualizes feature-matching results. Given a query point (indicated by a red star), the model trained with the InfoNCE loss exhibits cost-volume responses concentrated accurately around the correct corresponding location in the target view. Consequently, the predicted optical flow is highly accurate, enabling effective dense warping within the co-visible region, as illustrated by the clearly warped buildings in Fig. 15 (b). In contrast, the model trained without the InfoNCE loss yields dispersed responses throughout the image, leading to an incorrect regression position for the query point and ineffective dense warps, as shown in Fig. 15 (c) and (d).

5.4.2 Contributions from Architectures and Datasets

We attribute the powerful zero-shot generalization capability of PanMatch to two key factors: (1) domain-robust LVM representations, and (2) cross-task multi-domain training data. To validate this hypothesis, we systematically examine how these factors individually contribute to the baseline method’s performance on multiple benchmark matching tasks. In current study, DINOv2-reg-giant is adopted as the LVM encoder, and FlowFormer is selected as the unified matching baseline.

We conduct experiments to investigate: (i) whether LVM representations enhance domain generalization and cross-task adaptability when being trained on the same-scale dataset, (ii) whether the inclusion of additional optical flow data improves the baseline’s generalization, and (iii) whether incorporating cross-task data continues to benefit performance even when sufficient optical flow data (*i.e.*, 1M samples) is available.

TABLE 13: Comparison with the baseline under different training samples and feature backbone settings. Lower is better except for mAA. *OF* represents the collected flow datasets in Table 3.

ID	Datasets	Extractor	Flow		Stereo		Match WxBS mAA@10
			Sintel EPE	KITTI F1-All	Booster EPE	Middlebury Bad 2.0	
1	C+T	SVT-L	2.40	14.72	5.28	15.91	10.1
2	C+T+OF	SVT-L	2.29	8.28	5.10	14.51	12.3
3	Table 3	SVT-L	2.55	8.09	3.48	14.08	13.3
4	C+T	Ours	1.94	13.39	4.13	12.25	29.4
5	C+T+OF	Ours	1.69	5.68	3.18	8.94	16.5
6	Table 3	Ours	1.67	5.54	1.95	6.88	64.2

We answer these questions through quantitative evaluations on the optical flow datasets [51], [52], stereo matching datasets [88], [95] and feature matching benchmark [94]. Table 13 compares the baseline method with its LVM-augmented variant (Model 1 *vs.* 4, 2 *vs.* 5, and 3 *vs.* 6) on the same-scale datasets. These results demonstrate that LVM representations consistently enhance performance, not only for the original optical flow task but also in cross-task generalization. Besides, this advantage maintains across all training data scales. Moreover, while Model 3 exhibits degradation on Sintel and minimal improvement on WxBS, its LVM-augmented counterpart, Model 6, achieves significant gains across all evaluations. This contrast suggests that the baseline’s encoder struggles to learn general features from multi-task data, limiting overall performance. In contrast, LVM provides domain-invariant features, enabling broader data to further boost cross-task generalization for the matching module of baseline method.

On the other hand, comparisons between Models 1 & 2 or 4 & 5 indicate that incorporating larger amounts of optical flow data notably enhances optical flow and stereo matching accuracy. However, feature matching accuracy remains suboptimal, despite employing sufficient optical flow data (*e.g.*, 1M samples for Models 2 & 5). This limitation remains until cross-task datasets are integrated. As demonstrated by Models 5 & 6, adding cross-task data yields minimal improvement for optical flow generalization but significantly boosts cross-task generalization, particularly on the Booster dataset. This improvement stems primarily from the prevalence of non-Lambertian surfaces in Booster, which are underrepresented in existing optical flow simulation datasets. By generating optical flow samples from diverse datasets like Hypersim [12], our method effectively generalizes to such specialized scenarios, thereby confirming the value of cross-task data integration.

5.4.3 Framework Compatibility to Diverse Encoders

Our feature transformation pipeline is primarily designed for the plain multi-layer ViT architecture, therefore it is readily applied to recent foundation models, such as DINOv2 [66], SAM [71] and DAM [72]. We validate the compatibility of the adopter with various ViT pretraining weights in Table 14, confirming that all variants achieve state-of-the-art generalization performance. Notably, we observe that the model using DINOv2-Giant outperform that of using DINOv2-Base. This finding suggests that larger encoder capacity contributes to better zero-shot performance,

TABLE 14: Ablation for different encoders. FlowFormer is adopted as the baseline for flow estimation.

ID	Backbone	Dataset	KITTI F1-All	Sintel clean	Sintel final
0	Twins-SVT-L [125]	ImageNet-22k [126]	14.72	1.01	2.40
1	ConvNeXt-B [81]	ImageNet-22k [126]	14.49	1.14	2.71
2	Swin-B-224 ² [124]	ImageNet-22k [126]	15.89	1.20	2.65
3	SAM-B [71]	SAM-2B [71]	14.61	1.13	2.48
4	DAMv2-B [77]	DA-2B [77]	12.41	0.89	2.07
5	DINOv2-B [66]	LVM-142M [66]	13.40	1.02	2.21
6	DINOv2-G [66]	LVM-142M [66]	13.39	0.82	1.94

which aligns with the intuition that larger models possess stronger representation capabilities and more robust priors—both of which are crucial for downstream matching and aggregation processes involved in generalization.

Moreover, by employing the guided feature upsampling block to flexibly rescale features of arbitrary resolution to the required scale for feature pyramid construction, our transformation module supports diverse encoder architectures with varying output formats, such as multi-scale CNNs and Transformer-based models. To validate this compatibility, we employ ConvNeXt-B [81] and Swin-B [124] as frozen encoders, feeding stage-wise outputs into our module. However, this setup does not outperform the baseline configuration, which fine-tunes the ImageNet-pretrained Twins-SVT-L encoder [125]. We attribute this to the use of smaller-scale backbones and the inefficiency of side-tuning compared to direct encoder fine-tuning. Nevertheless, direct tuning may be impractical for ViT architectures due to their vast parameter sizes and data demands.

We should emphasize that our primary objective in this study is to evaluate the effectiveness and generality of the proposed adopter across different architectures and pretrained weights. Given that different pretrained weights stem from varying training strategies and datasets, direct comparisons between pyramid and plain encoders for zero-shot performance would be unfair. Therefore, we omit such comparisons and instead focus on demonstrating the framework’s generality. In practice, we adopt DINOv2 as the frozen LVM encoder for PanMatch, as it shows the best generalization performance in our current studies.

5.5 Real-World Application

Given a video sequence or sparse multi-view images, our method directly estimates per-frame depth maps without relying on pose priors. This is achieved by first generating the unified displacement field. Then, the confidence-filtered dense correspondences are used to estimate relative camera poses, enabling subsequent depth calculation. As illustrated in Fig. 16, we back-project these per-frame depth estimates into a common world coordinate system for point cloud registration and fusion. The resulting fused point cloud captures the scene geometry across multiple views, demonstrating geometrically coherent reconstruction. These results validate the robust performance and strong cross-task capabilities of our approach.

6 CONCLUSION

In this work, we present *PanMatch*, a versatile model designed to address diverse correspondence tasks. This multi-

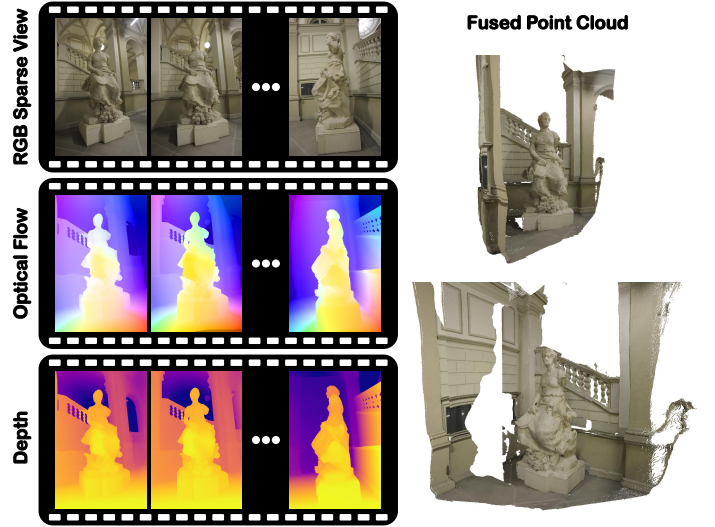


Fig. 16: A unique task that the independent methods are unable to solve. Given a traveling video, our model can infer the depth without the need of pose information.

task capability stems from two key designs: (1) a unified 2D displacement field representation, and (2) a zero-shot generalization strategy implemented by integrating domain-invariant representations from LVMs and pretraining on multi-domain datasets. To effectively adapt LVM features for correspondence tasks, we develop a Feature Transformation pipeline that extracts a multi-scale feature pyramid from the LVM representations. Furthermore, we reorganize various datasets with task-specific annotation formats (*e.g.*, disparity, depth, and flow) into a common dense displacement field, enabling the aggregation of multi-domain and multi-task datasets for large-scale pretraining. Extensive experiments demonstrate that PanMatch achieves state-of-the-art or highly competitive performance across 15 popular benchmarks for flow, stereo, depth and feature matching, underscoring its multitasking versatility and cross-domain generalization.

A key insight of this work is that any two-frame matching task can be effectively addressed under a single paradigm of 2D displacement field prediction. This formulation not only unifies various correspondence matching tasks but also facilitates pretraining with datasets from diverse sources. We hope our findings will be valuable for advancing dense correspondence and multi-view perception tasks.

ACKNOWLEDGE

This work was partially supported by the National Natural Science Foundation of China (No. 62301601, U20A20185, 62372491), the Guangdong Basic and Applied Basic Research Foundation (2022B1515020103, 2023B1515120087), the Shenzhen Science and Technology Program (No. RCYX20200714114641140).

REFERENCES

- [1] H. Xu, J. Zhang, J. Cai, H. Rezatofighi, F. Yu, D. Tao, and A. Geiger, “Unifying flow, stereo and depth estimation,” *IEEE Trans. Pattern Anal. Mach. Intell.*, 2023.

- [2] S. Zhang, X. Sun, H. Chen, B. Li, and C. Shen, "RGM: A robust generalizable matching model," *arXiv:2310.11755*, 2023.
- [3] J. Wang, M. Chen, N. Karaev, A. Vedaldi, C. Rupprecht, and D. Novotny, "VGGT: Visual geometry grounded transformer," in *CVPR*, 2025.
- [4] W. Chuah, R. B. Tennakoon, R. Hoseinnezhad, A. Bab-Hadiashar, and D. Suter, "ITSA: An information-theoretic approach to automatic shortcut avoidance and domain generalization in stereo matching networks," in *CVPR*, 2022.
- [5] J. Li, P. Wang, P. Xiong, T. Cai, Z. Yan, L. Yang, J. Liu, H. Fan, and S. Liu, "Practical stereo matching via cascaded recurrent network with adaptive correlation," in *CVPR*, 2022.
- [6] J. Tremblay, T. To, and S. Birchfield, "Falling Things: A synthetic dataset for 3D object detection and pose estimation," in *CVPR Workshops*, 2018.
- [7] N. Mayer, E. Ilg, P. Häusser, P. Fischer, D. Cremers, A. Dosovitskiy, and T. Brox, "A large dataset to train convolutional networks for disparity, optical flow, and scene flow estimation," in *CVPR*, 2016.
- [8] A. Dosovitskiy, P. Fischer, E. Ilg, P. Häusser, C. Hazirbas, V. Golkov, P. van der Smagt, D. Cremers, and T. Brox, "FlowNet: Learning optical flow with convolutional networks," in *ICCV*, 2015.
- [9] D. Sun, D. Vlasic, C. Herrmann, V. Jampani, M. Krainin, H. Chang, R. Zabih, W. T. Freeman, and C. Liu, "AutoFlow: Learning a better training set for optical flow," in *CVPR*, 2021.
- [10] Y. Cabon, N. Murray, and M. Humenberger, "Virtual KITTI 2," 2020.
- [11] W. Wang, D. Zhu, X. Wang, Y. Hu, Y. Qiu, C. Wang, Y. Hu, A. Kapoor, and S. A. Scherer, "Tartanair: A dataset to push the limits of visual SLAM," in *IROS*, 2020.
- [12] M. Roberts, J. Ramapuram, A. Ranjan, A. Kumar, M. Á. Bautista, N. Paczan, R. Webb, and J. M. Susskind, "Hypersim: A photorealistic synthetic dataset for holistic indoor scene understanding," in *ICCV*, 2021.
- [13] Z. Li and N. Snavely, "MegaDepth: Learning single-view depth prediction from internet photos," in *CVPR*, 2018.
- [14] P. Weinzaepfel, T. Lucas, V. Leroy, Y. Cabon, V. Arora, R. Brégier, G. Csurka, L. Antsfeld, B. Chidlovskii, and J. Revaud, "CroCo v2: Improved cross-view foundation pre-training for stereo matching and optical flow," in *ICCV*, 2023.
- [15] X. Guo, C. Zhang, Y. Zhang, D. Nie, R. Wang, W. Zheng, M. Poggi, and L. Chen, "Stereo Anything: Unifying stereo matching with large-scale mixed data," *arXiv:2411.14053*, 2024.
- [16] B. Wen, M. Trepte, J. Aribido, J. Kautz, O. Gallo, and S. Birchfield, "FoundationStereo: Zero-shot stereo matching," in *CVPR*, 2025.
- [17] Y. Zhang, L. Wang, K. Li, Y. Wang, and Y. Guo, "Learning representations from foundation models for domain generalized stereo matching," in *ECCV*, 2025.
- [18] M. Poggi, F. Tosi, K. Batsos, P. Mordohai, and S. Mattoccia, "On the synergies between machine learning and binocular stereo for depth estimation from images: A survey," *IEEE Trans. Pattern Anal. Mach. Intell.*, 2022.
- [19] H. Laga, L. V. Jospin, F. Boussaid, and M. Bennamoun, "A survey on deep learning techniques for stereo-based depth estimation," *IEEE Trans. Pattern Anal. Mach. Intell.*, 2022.
- [20] J. Zbontar and Y. LeCun, "Computing the stereo matching cost with a convolutional neural network," in *CVPR*, 2015.
- [21] A. Seki and M. Pollefeys, "SGM-Nets: Semi-global matching with neural networks," in *CVPR*, 2017.
- [22] D. Scharstein and R. Szeliski, "A taxonomy and evaluation of dense two-frame stereo correspondence algorithms," *Int. J. Comput. Vis.*, 2002.
- [23] H. Hirschmüller, "Accurate and efficient stereo processing by semi-global matching and mutual information," in *CVPR*, 2005.
- [24] J. Chang and Y. Chen, "Pyramid stereo matching network," in *CVPR*, 2018.
- [25] F. Zhang, V. A. Prisacariu, R. Yang, and P. H. S. Torr, "GANet: Guided aggregation net for end-to-end stereo matching," in *CVPR*, 2019.
- [26] H. Xu and J. Zhang, "AANet: Adaptive aggregation network for efficient stereo matching," in *CVPR*, 2020.
- [27] G. Xu, J. Cheng, P. Guo, and X. Yang, "Attention concatenation volume for accurate and efficient stereo matching," in *CVPR*, 2022.
- [28] Z. Liang, Y. Guo, Y. Feng, W. Chen, L. Qiao, L. Zhou, J. Zhang, and H. Liu, "Stereo matching using multi-level cost volume and multi-scale feature constancy," *IEEE Trans. Pattern Anal. Mach. Intell.*, 2021.
- [29] G. Yang, J. Manela, M. Happold, and D. Ramanan, "Hierarchical deep stereo matching on high-resolution images," in *CVPR*, 2019.
- [30] G. Xu, Y. Wang, J. Cheng, J. Tang, and X. Yang, "Accurate and efficient stereo matching via attention concatenation volume," *IEEE Trans. Pattern Anal. Mach. Intell.*, 2024.
- [31] V. Tankovich, C. Hane, Y. Zhang, A. Kowdle, S. R. Fanello, and S. Bouaziz, "HITNet: Hierarchical iterative tile refinement network for real-time stereo matching," in *CVPR*, 2021.
- [32] G. Xu, X. Wang, Z. Zhang, J. Cheng, C. Liao, and X. Yang, "IGEV++: Iterative multi-range geometry encoding volumes for stereo matching," *IEEE Trans. Pattern Anal. Mach. Intell.*, 2025.
- [33] Z. Teed and J. Deng, "RAFT: recurrent all-pairs field transforms for optical flow," in *ECCV*, 2020.
- [34] L. Lipson, Z. Teed, and J. Deng, "RAFT-Stereo: Multilevel recurrent field transforms for stereo matching," in *3DV*, 2021.
- [35] G. Xu, X. Wang, X. Ding, and X. Yang, "Iterative geometry encoding volume for stereo matching," in *CVPR*, 2023.
- [36] X. Wang, G. Xu, H. Jia, and X. Yang, "Selective-Stereo: Adaptive frequency information selection for stereo matching," in *CVPR*, 2024.
- [37] F. Zhang, X. Qi, R. Yang, V. Prisacariu, B. W. Wah, and P. H. S. Torr, "Domain-invariant stereo matching networks," in *ECCV*, 2020.
- [38] C. Cai, M. Poggi, S. Mattoccia, and P. Mordohai, "Matching-space stereo networks for cross-domain generalization," in *3DV*, 2020.
- [39] B. Liu, H. Yu, and G. Qi, "GraftNet: Towards domain generalized stereo matching with a broad-spectrum and task-oriented feature," in *CVPR*, 2022.
- [40] J. Zhang, X. Wang, X. Bai, C. Wang, L. Huang, Y. Chen, L. Gu, J. Zhou, T. Harada, and E. R. Hancock, "Revisiting domain generalized stereo matching networks from a feature consistency perspective," in *CVPR*, 2022.
- [41] W. Chuah, R. B. Tennakoon, R. Hoseinnezhad, D. Suter, and A. Bab-Hadiashar, "An information-theoretic method to automatic shortcut avoidance and domain generalization for dense prediction tasks," *IEEE Trans. Pattern Anal. Mach. Intell.*, 2023.
- [42] T. Chang, X. Yang, T. Zhang, and M. Wang, "Domain generalized stereo matching via hierarchical visual transformation," in *CVPR*, 2023.
- [43] Z. Rao, B. Xiong, M. He, Y. Dai, R. He, Z. Shen, and X. Li, "Masked representation learning for domain generalized stereo matching," in *CVPR*, 2023.
- [44] A. S. Wannenwetsch, M. Keuper, and S. Roth, "ProbFlow: Joint optical flow and uncertainty estimation," in *ICCV*, 2017.
- [45] D. Sun, X. Yang, M. Liu, and J. Kautz, "PWC-Net: Cnns for optical flow using pyramid, warping, and cost volume," in *CVPR*, 2018.
- [46] E. Ilg, N. Mayer, T. Saikia, M. Keuper, A. Dosovitskiy, and T. Brox, "FlowNet 2.0: Evolution of optical flow estimation with deep networks," in *CVPR*, 2017.
- [47] S. Jiang, D. Campbell, Y. Lu, H. Li, and R. I. Hartley, "Learning to estimate hidden motions with global motion aggregation," in *ICCV*, 2021.
- [48] Y. Wang, L. Lipson, and J. Deng, "SEA-RAFT: simple, efficient, accurate RAFT for optical flow," in *ECCV*, 2024.
- [49] H. Xu, J. Zhang, J. Cai, H. Rezatofighi, and D. Tao, "GMFlow: Learning optical flow via global matching," in *CVPR*, 2022.
- [50] Z. Huang, X. Shi, C. Zhang, Q. Wang, K. C. Cheung, H. Qin, J. Dai, and H. Li, "FlowFormer: A transformer architecture for optical flow," in *ECCV*, 2022.
- [51] D. J. Butler, J. Wulff, G. B. Stanley, and M. J. Black, "A naturalistic open source movie for optical flow evaluation," in *ECCV*, 2012.
- [52] M. Menze, C. Heipke, and A. Geiger, "Object scene flow," *ISPRS J. Photogramm. Remote Sens.*, 2018.
- [53] S. R. Richter, Z. Hayder, and V. Koltun, "Playing for benchmarks," in *ICCV*, 2017.
- [54] A. Geiger, P. Lenz, and R. Urtasun, "Are we ready for autonomous driving? The KITTI vision benchmark suite," in *CVPR*, 2012.
- [55] K. Greff, F. Belletti, L. Beyer, C. Doersch, Y. Du, D. Duckworth, D. J. Fleet, D. Gnanaprasadam, F. Golemo, C. Herrmann, T. Kipf, A. Kundu, D. Lagun, I. H. Laradji, H. D. Liu, H. Meyer, Y. Miao, D. Nowrouzezahrai, A. C. Öztireli, E. Pot, N. Radwan, D. Rebain, S. Sabour, M. S. M. Sajjadi, M. Sela, V. Sitzmann, A. Stone, D. Sun, S. Vora, Z. Wang, T. Wu, K. M. Yi, F. Zhong, and A. Tagliasacchi, "Kubric: A scalable dataset generator," in *CVPR*, 2022.

- [56] K. M. Yi, E. Trulls, V. Lepetit, and P. Fua, "LIFT: learned invariant feature transform," in *ECCV*, 2016.
- [57] D. DeTone, T. Malisiewicz, and A. Rabinovich, "SuperPoint: Self-supervised interest point detection and description," in *CVPR Workshops*, 2018.
- [58] P. Sarlin, D. DeTone, T. Malisiewicz, and A. Rabinovich, "SuperGlue: Learning feature matching with graph neural networks," in *CVPR*, 2020.
- [59] K. Li, L. Wang, L. Liu, Q. Ran, K. Xu, and Y. Guo, "Decoupling makes weakly supervised local feature better," in *CVPR*, 2022.
- [60] I. Rocco, R. Arandjelović, and J. Sivic, "Efficient neighbourhood consensus networks via submanifold sparse convolutions," in *ECCV*, 2020.
- [61] X. Li, K. Han, S. Li, and V. Prisacariu, "Dual-resolution correspondence networks," in *NeurIPS*, 2020.
- [62] J. Sun, Z. Shen, Y. Wang, H. Bao, and X. Zhou, "LoFTR: Detector-free local feature matching with transformers," in *CVPR*, 2021.
- [63] J. Edstedt, Q. Sun, G. Bökman, M. Wadenbäck, and M. Felsberg, "RoMa: Robust dense feature matching," in *CVPR*, 2024.
- [64] J. Edstedt, I. Athanasiadis, M. Wadenbäck, and M. Felsberg, "DKM: dense kernelized feature matching for geometry estimation," in *CVPR*, 2023.
- [65] Z. Shen, J. Sun, Y. Wang, X. He, H. Bao, and X. Zhou, "Semi-dense feature matching with transformers and its applications in multiple-view geometry," *IEEE Trans. Pattern Anal. Mach. Intell.*, 2023.
- [66] M. Oquab, T. Darcet, T. Moutakanni, H. V. Vo, M. Szafraniec, V. Khalidov, P. Fernandez, D. Haziza, F. Massa, A. El-Nouby, R. Howes, P.-Y. Huang, H. Xu, V. Sharma, S.-W. Li, W. Galuba, M. Rabbat, M. Assran, N. Ballas, G. Synnaeve, I. Misra, H. Jegou, J. Mairal, P. Labatut, A. Joulin, and P. Bojanowski, "DINOv2: Learning robust visual features without supervision," *arXiv:2304.07193*, 2023.
- [67] Z. Yin, T. Darrell, and F. Yu, "Hierarchical discrete distribution decomposition for match density estimation," in *CVPR*, 2019.
- [68] P. Truong, M. Danelljan, L. V. Gool, and R. Timofte, "Learning accurate dense correspondences and when to trust them," in *CVPR*, 2021.
- [69] P. Truong, M. Danelljan, R. Timofte, and L. V. Gool, "PDC-Net+: Enhanced probabilistic dense correspondence network," *IEEE Trans. Pattern Anal. Mach. Intell.*, 2023.
- [70] A. Radford, J. W. Kim, C. Hallacy, A. Ramesh, G. Goh, S. Agarwal, G. Sastry, A. Askell, P. Mishkin, J. Clark, G. Krueger, and I. Sutskever, "Learning transferable visual models from natural language supervision," in *ICML*, 2021.
- [71] A. Kirillov, E. Mintun, N. Ravi, H. Mao, C. Rolland, L. Gustafson, T. Xiao, S. Whitehead, A. C. Berg, W.-Y. Lo *et al.*, "Segment anything," *arXiv:2304.02643*, 2023.
- [72] L. Yang, B. Kang, Z. Huang, X. Xu, J. Feng, and H. Zhao, "Depth Anything: Unleashing the power of large-scale unlabeled data," in *CVPR*, 2024.
- [73] Z. Chen, Y. Duan, W. Wang, J. He, T. Lu, J. Dai, and Y. Qiao, "Vision transformer adapter for dense predictions," in *ICLR*, 2023.
- [74] Z. Zhong, Z. Tang, T. He, H. Fang, and C. Yuan, "Convolution meets lora: Parameter efficient finetuning for segment anything model," in *ICLR*, 2024.
- [75] C.-W. Liu, Q. Chen, and R. Fan, "Playing to vision foundation model's strengths in stereo matching," *arXiv:2404.06261*, 2024.
- [76] L. Bartolomei, F. Tosi, M. Poggi, and S. Mattoccia, "Stereo Anywhere: Robust zero-shot deep stereo matching even where either stereo or mono fail," in *CVPR*, 2025.
- [77] L. Yang, B. Kang, Z. Huang, Z. Zhao, X. Xu, J. Feng, and H. Zhao, "Depth Anything V2," in *NeurIPS*, 2024.
- [78] S. Zhou, R. He, W. Tan, and B. Yan, "SAMFlow: Eliminating any fragmentation in optical flow with segment anything model," in *AAAI*, 2024.
- [79] M. D. Zeiler, D. Krishnan, G. W. Taylor, and R. Fergus, "Deconvolutional networks," in *CVPR*, 2010.
- [80] A. Vaswani, N. Shazeer, N. Parmar, J. Uszkoreit, L. Jones, A. N. Gomez, L. Kaiser, and I. Polosukhin, "Attention is all you need," in *NeurIPS*, 2017.
- [81] Z. Liu, H. Mao, C.-Y. Wu, C. Feichtenhofer, T. Darrell, and S. Xie, "A ConvNet for the 2020s," *CVPR*, 2022.
- [82] K. He, H. Fan, Y. Wu, S. Xie, and R. B. Girshick, "Momentum contrast for unsupervised visual representation learning," in *CVPR*, 2020.
- [83] N. Karaev, I. Rocco, B. Graham, N. Neverova, A. Vedaldi, and C. Rupprecht, "DynamicStereo: Consistent dynamic depth from stereo videos," in *CVPR*, 2023.
- [84] G. Wu, X. Liu, K. Luo, X. Liu, Q. Zheng, S. Liu, X. Jiang, G. Zhai, and W. Wang, "AccFlow: Backward accumulation for long-range optical flow," in *ICCV*, 2023.
- [85] T. Darcet, M. Oquab, J. Mairal, and P. Bojanowski, "Vision transformers need registers," in *ICLR*, 2024.
- [86] I. Loshchilov and F. Hutter, "Decoupled weight decay regularization," in *ICLR*, 2019.
- [87] Y. Liang, Y. Fu, Y. Hu, W. Shao, J. Liu, and D. Zhang, "Flow-Anything: Learning real-world optical flow estimation from large-scale single-view images," *IEEE Trans. Pattern Anal. Mach. Intell.*, 2025.
- [88] D. Scharstein, H. Hirschmüller, Y. Kitajima, G. Krathwohl, N. Nesić, X. Wang, and P. Westling, "High-resolution stereo datasets with subpixel-accurate ground truth," in *GCPR*, 2014.
- [89] T. Schops, J. L. Schonberger, S. Galliani, T. Sattler, K. Schindler, M. Pollefeys, and A. Geiger, "A multi-view stereo benchmark with high-resolution images and multi-camera videos," in *CVPR*, 2017.
- [90] A. Raistrick, L. Lipson, Z. Ma, L. Mei, M. Wang, Y. Zuo, K. Kayan, H. Wen, B. Han, Y. Wang, A. Newell, H. Law, A. Goyal, K. Yang, and J. Deng, "Infinite photorealistic worlds using procedural generation," in *CVPR*, 2023.
- [91] L. Mehl, J. Schmalzuss, A. Jahedi, Y. Nalivayko, and A. Bruhn, "Spring: A high-resolution high-detail dataset and benchmark for scene flow, optical flow and stereo," in *CVPR*, 2023.
- [92] A. Dai, A. X. Chang, M. Savva, M. Halber, T. A. Funkhouser, and M. Nießner, "ScanNet: Richly-annotated 3D reconstructions of indoor scenes," in *CVPR*, 2017.
- [93] B. Thomee, D. A. Shamma, G. Friedland, B. Elizalde, K. Ni, D. Poland, D. Borth, and L. Li, "YFCC100M: the new data in multimedia research," *Commun. ACM*, 2016.
- [94] D. Mishkin, J. Matas, M. Perdoch, and K. Lenc, "WxBS: Wide baseline stereo generalizations," in *BMVC*, 2015.
- [95] P. Z. Ramirez, F. Tosi, M. Poggi, S. Salti, S. Mattoccia, and L. D. Stefano, "Open challenges in deep stereo: the Booster dataset," in *CVPR*, 2022.
- [96] M. Allan, J. Mcleod, C. Wang, J. C. Rosenthal, Z. Hu, N. Gard, P. Eisert, K. X. Fu, T. Zeffiro, W. Xia *et al.*, "Stereo correspondence and reconstruction of endoscopic data challenge," *arXiv:2101.01133*, 2021.
- [97] G. Yang, X. Song, C. Huang, Z. Deng, J. Shi, and B. Zhou, "DrivingStereo: A large-scale dataset for stereo matching in autonomous driving scenarios," in *CVPR*, 2019.
- [98] J. Xiao, A. Owens, and A. Torralba, "SUN3D: A database of big spaces reconstructed using sfm and object labels," in *ICCV*, 2013.
- [99] J. Sturm, N. Engelhard, F. Endres, W. Burgard, and D. Cremers, "A benchmark for the evaluation of RGB-D SLAM systems," in *IROS*, 2012.
- [100] Y. Wang, L. Wang, J. Yang, W. An, and Y. Guo, "Flickr1024: A large-scale dataset for stereo image super-resolution," in *CVPR Workshops*, 2019.
- [101] A. Jahedi, M. Luz, M. Rivinius, L. Mehl, and A. Bruhn, "MS-RAFT+: high resolution multi-scale raft," *Int. J. Comput. Vis.*, 2024.
- [102] Y. Miao, M. Wu, S. K. Lam, C. Li, and T. Srikanthan, "Hierarchical object-aware dual-level contrastive learning for domain generalized stereo matching," in *NeurIPS*, 2024.
- [103] P. Xu, Z. Xiang, C. Qiao, J. Fu, and T. Pu, "Adaptive multi-modal cross-entropy loss for stereo matching," in *CVPR*, 2024.
- [104] X. Shi, Z. Huang, D. Li, M. Zhang, K. C. Cheung, S. See, H. Qin, J. Dai, and H. Li, "FlowFormer++: Masked cost volume autoencoding for pretraining optical flow estimation," in *CVPR*, 2023.
- [105] S. Sun, Y. Chen, Y. Zhu, G. Guo, and G. Li, "SKFlow: Learning optical flow with super kernels," in *NeurIPS*, 2022.
- [106] A. Jahedi, M. Luz, M. Rivinius, and A. Bruhn, "CCMR: High resolution optical flow estimation via coarse-to-fine context-guided motion reasoning," in *WACV*, 2024.
- [107] Q. Dong, C. Cao, and Y. Fu, "Rethinking optical flow from geometric matching consistent perspective," in *CVPR*, 2023.
- [108] Z. Rao, M. He, Y. Dai, Z. Zhu, B. Li, and R. He, "NLCA-Net: a non-local context attention network for stereo matching," *APSIPA Trans. Signal Inf. Process.*, 2020.
- [109] Z. Shen, Y. Dai, and Z. Rao, "CFNet: Cascade and fused cost volume for robust stereo matching," in *CVPR*, 2021.

- [110] Z. Shen, X. Song, Y. Dai, D. Zhou, Z. Rao, and L. Zhang, "Digging into uncertainty-based pseudo-label for robust stereo matching," *IEEE Trans. Pattern Anal. Mach. Intell.*, 2023.
- [111] H. Jiang, R. Xu, and W. Jiang, "An improved raftstereo trained with a mixed dataset for the robust vision challenge 2022," *arXiv:2210.12785*, 2022.
- [112] J. Jing, J. Li, P. Xiong, J. Liu, S. Liu, Y. Guo, X. Deng, M. Xu, L. Jiang, and L. Sigal, "Uncertainty guided adaptive warping for robust and efficient stereo matching," in *ICCV*, 2023.
- [113] K. Li, L. Wang, Y. Zhang, K. Xue, S. Zhou, and Y. Guo, "LoS: Local structure-guided stereo matching," in *CVPR*, 2024.
- [114] H. Jiang, Z. Lou, L. Ding, R. Xu, M. Tan, W. Jiang, and R. Huang, "DEFOM-Stereo: Depth foundation model based stereo matching," *arXiv:2501.09466*, 2025.
- [115] D. Sun, C. Herrmann, F. A. Reda, M. Rubinstein, D. J. Fleet, and W. T. Freeman, "Disentangling architecture and training for optical flow," in *ECCV*, 2022.
- [116] P. Z. Ramirez, A. Costanzino, F. Tosi, M. Poggi, S. Salti, S. Mattoccia, and L. D. Stefano, "Booster: A benchmark for depth from images of specular and transparent surfaces," *IEEE Trans. Pattern Anal. Mach. Intell.*, 2024.
- [117] W. Maddern, G. Pascoe, C. Linegar, and P. Newman, "1 year, 1000 km: The oxford robotcar dataset," *The International Journal of Robotics Research*, 2017.
- [118] M. Bosch, K. Foster, G. Christie, S. Wang, G. D. Hager, and M. Brown, "Semantic stereo for incidental satellite images," in *WACV*, 2019.
- [119] H. Chen, Z. Luo, L. Zhou, Y. Tian, M. Zhen, T. Fang, D. McKinnon, Y. Tsin, and L. Quan, "ASpanFormer: Detector-free image matching with adaptive span transformer," in *ECCV*, 2022.
- [120] B. Ummenhofer, H. Zhou, J. Uhrig, N. Mayer, E. Ilg, A. Dosovitskiy, and T. Brox, "DeMoN: Depth and motion network for learning monocular stereo," in *CVPR*, 2017.
- [121] P.-H. Huang, K. Matzen, J. Kopf, N. Ahuja, and J.-B. Huang, "DeepMVS: Learning multi-view stereopsis," in *CVPR*, 2018.
- [122] S. Im, H. Jeon, S. Lin, and I. S. Kweon, "DPSNet: End-to-end deep plane sweep stereo," in *ICLR*, 2019.
- [123] W. Yifan, C. Doersch, R. Arandjelović, J. a. Carreira, and A. Zisserman, "Input-level inductive biases for 3D reconstruction," in *CVPR*, 2022.
- [124] Z. Liu, Y. Lin, Y. Cao, H. Hu, Y. Wei, Z. Zhang, S. Lin, and B. Guo, "Swin Transformer: Hierarchical vision transformer using shifted windows," in *ICCV*, 2021.
- [125] X. Chu, Z. Tian, Y. Wang, B. Zhang, H. Ren, X. Wei, H. Xia, and C. Shen, "Twins: Revisiting the design of spatial attention in vision transformers," in *NeurIPS*, 2021.
- [126] J. Deng, W. Dong, R. Socher, L.-J. Li, K. Li, and L. Fei-Fei, "ImageNet: A large-scale hierarchical image database," in *CVPR*, 2009.



Yongjian Zhang received the B.Eng. degree from Sun Yat-sen University (SYSU) in 2021, where he is currently pursuing the Ph.D. degree with the School of Electronics and Communication Engineering. His current research interests focus on stereo matching, depth estimation and completion, and vision-and-language navigation.



Longguang Wang received the B.E. degree in Electrical Engineering from Shandong University (SDU), Jinan, China, in 2015, and the Ph.D. degree in Information and Communication Engineering from National University of Defense Technology (NUDT), Changsha, China, in 2022. His current research interests include low-level vision and 3D vision.



Kunhong Li received the B.Eng. degree from Xiamen University (XMU) in 2017 and the M.Eng. degree from Sun Yat-sen University (SYSU), China, in 2021, where he is currently pursuing the Ph.D. degree with the School of Electronics and Communication Engineering. His current research interests focus on 3D reconstruction, local feature extraction, and depth estimation.



Yun Wang received the B.E. degree from China University of Geosciences (CUG) in 2020 and the M.E. degree from Sun Yat-sen University (SYSU), China, in 2023. He is currently pursuing the Ph.D. degree with the Department of Computer Science, City University of Hong Kong, Hong Kong SAR. His current research interests include deep learning and 3D vision, especially depth estimation.



Ye Zhang received the Ph.D. degree in Electronic Science and Technology from National University of Defense Technology (NUDT), Changsha, China, in 2023. He served as a post-doctor at Sun Yat-sen University (SYSU) from 2023 to 2024. He is currently an associate researcher of the School of Electronics and Communication Engineering, Sun Yat-sen University, Shenzhen, China. His main research interests include 3D vision and human-computer interaction.



Liang Lin (Fellow, IEEE) is a Full Professor of computer science at Sun Yat-sen University. He served as the Executive Director and Distinguished Scientist of SenseTime Group from 2016 to 2018, leading the R&D teams for cutting-edge technology transferring. He has authored or co-authored more than 200 papers in leading academic journals and conferences, and his papers have been cited by more than 30,000 times. He is an associate editor of *IEEE Trans. Neural Networks and Learning Systems* and *IEEE Trans. Multimedia*, and served as Area Chairs for numerous conferences such as CVPR, ICCV, SIGKDD and AAAI. He is the recipient of numerous awards and honors including Wu Wen-Jun Artificial Intelligence Award, the First Prize of China Society of Image and Graphics, ICCV Best Paper Nomination in 2019, Annual Best Paper Award by Pattern Recognition (Elsevier) in 2018, Best Paper Diamond Award in IEEE ICME 2017, Google Faculty Award in 2012. His supervised PhD students received ACM China Doctoral Dissertation Award, CCF Best Doctoral Dissertation and CAAI Best Doctoral Dissertation. He is a Fellow of IEEE/IAPR/IET.



Yulan Guo is a full Professor with Sun Yat-sen University. He has authored over 200 articles at highly referred journals and conferences, receiving over 20,000 citations in Google Scholar. His research interests lie in spatial intelligence, 3D vision, and robotics. He served as a Senior Area Editor for *IEEE Transactions on Image Processing*, and an Associate Editor for the *Visual Computer*, and *Computers & Graphics*. He also served as an area chair for CVPR 2025/2023/2021, ICCV 2025/2021, ECCV 2024,

NeurIPS 2024, and ACM Multimedia 2021. He organized over 10 workshops, challenges, and tutorials in prestigious conferences such as CVPR, ICCV, ECCV, and 3DV. He is a Senior Member of IEEE and ACM.